UC Merced
UC Merced Electronic Theses and Dissertations

Title

Fluid-Structure Interaction of Slender Biofilaments at Low Reynolds Numbers

Permalink

https://escholarship.org/uc/item/96f5z875

Author

Mortazavi, Mehrad

Publication Date

2020

Copyright Information

Peer reviewed|Thesis/dissertation

University of California, Merced

Fluid-Structure Interaction of Slender Biofilaments at Low Reynolds Numbers

A thesis submitted in partial satisfaction of the requirements for the degree of
Master of Science

in

Mechanical Engineering

by

Mehrad Mortazavi

Committee in charge:

Professor Sachin Goyal, Chair
Professor Arvind Gopinath
Professor Francois Blanchette
Professor Venkattraman Ayyaswamy

2020

I would love to dedicate this thesis to my parents, siblings, close friends, and advisers whose overwhelming support helped me overcome all the barriers throughout my postgraduate journey.

Contents

List of Figures

Acknowledgments

Abstract

Some hair-like biofilaments such as cilia and flagella, experience structural instability that results in complex dynamic behaviors. They deform due to active shearing or movement of molecular motors along the filament. This is also a reason for the wave-like motion of the microorganism in its surrounding fluid. Predicting the beating pattern of such elastic slender filaments in a dissipative viscous liquid at low Reynolds numbers requires a robust computational model that can both capture the dynamics of an elastic filament as well as the hydrodynamic interactions between the structure and the fluid. To address such an elastohydrodynamic problem, we have developed a computational rod model to capture the structural dynamics of an elastic filament. We then use slender body theory (SBT) to determine the hydrodynamic interactions of the filament with the viscous fluid and combine it with our computational rod model. At low Reynolds numbers where the Stokes equations govern the motion of the fluid, viscous forces are dominant over inertial forces, which results in a linear relationship between the hydrodynamic drag force and the cross-sectional velocity of the filament. However, depending on the shape of the filament, the drag coefficient on each cross-section can vary along the centerline. Not only the shape but the presence of other no-slip boundaries such as a rigid plane wall or another nearby slender object can affect both the magnitude and the distribution of the hydrodynamic drag force across the centerline of the filament. However, the SBT model is capable of handling such nonlocal hydrodynamic interactions between the filament, the wall, and the fluid. We provide an iterative spatio-temporal procedure through which we obtain the hydrodynamic drag forces and the shape of the filament at each time step. The fluid-structure interaction model presented here can be used to mimic the motion of actual cilia, flagella. However, as an additional contribution, we analyzed the accuracy of the slender body formulations. Although SBT is computationally faster than other hydrodynamic drag models, it may not provide accurate solutions for filaments with a small length-over-radius ratio. Thus, to estimate the error associated with the SBT at different slenderness ratios, we employ a computational fluid dynamic solver (CFD) and compare the results.

Chapter 1

Introduction

1.1 Motivation

Active matter systems are groups of active agents, consuming energy and converting it into mechanical energy. For instance, a flock of birds, a swarm of bees, bacteria colonies, and actin-myosin-based systems are all considered as active matter[76, 72, 86]. In the active matter systems, each component is separately active and interacts with its surrounding environment. To understand active matter and their collective behavior, one approach is to study single active components. On small scales, microorganisms are considered as single active agents. They are interesting for biomedical studies and investigation of them is a natural step towards making synthetic prototypes. There are also many potential applications in drug delivery and programmable systems [30, 68, 71].

Many microorganisms such as bacteria [60], planktons [41], cilia and flagella [97], and spermatozoa [33] can be modeled as slender particles swimming through a viscous environment. Flagella and cilia are organelles found in humans and most of the mammalian cells. It has been observed that such hair-like filaments demonstrate regular beating and rotating patterns due to the sophisticated activity inside their microtubule-based structure called axoneme [49, 75]. The sliding motion of motor proteins called dynein along the filament induces shearing between the cross-linked microtubules and forces the structure to bend and buckle [96, 100, 79]. The follower forces are imposed to the structure due to the back-and-forth movement of dynein arms along the filament are a reason for the wavelike motion of flagella or cilia in its surrounding fluid. Malfunctioning of cilia or flagella in the body can cause a wide range of issues such as blindness, syndromic developmental disorders, polycystic kidney disease, infertility, and olfactory disorders and many more [1, 13]. Therefore, a thorough understanding of their working mechanism can help human to prevent a lot of health-threatening problems [46, 93, 2, 6, 7].

Although many research studies on cilia and flagella are conducted in cellular and biological contexts, mimicking their beating patterns has given rise to new applications in drug delivery, microfluidic devices, and cargo transport [75, 74, 14]. The research on artificial cilia started less than two decades ago and is attracting more attention every year [98, 37]. In a recent study by [44], synthetic magnetic cilia are fabricated and planted in multi-row arrays within the microchannels. Inducing the ciliary arrays by a rotating magnet can force the fluid to be propelled through the microchannels. Surface fouling is a problem that affects most of the lab-on-chip devices and marine sensors. Thanks to the versatility of the cilia in the manipulation of fluids and particles, artificially ciliating the surfaces can advert the attachment of biofouling agents and stop their sedimentation on the surface of interest[107, 106, 108, 87]. The actuation of the magnetic artificial cilia can be used as a self-cleaning and antifouling strategy with up to 99% of efficiency[107].

The motivation for understanding the dynamics of micro-swimmers and slender bio-filaments such as flagella and cilia in the fluid has given rise to many mathematical modelings [26]. Those models have continuously attempted to discover: What correlation is between the beating patterns and the force generation mechanism of a cilium or flagellum? By which mechanism the collective beating patterns of cilia produce metachronal waves? What are the reasons for the stability of the metachronal waves? What are the relationships between the frequency of oscillations and the movement of molecular motors? What are the mechanical properties of the cilia/flagella and how do they depend on the frequency and amplitude of the beating patterns?[104, 24, 70, 57, 25, 88, 91] Advances in computing technology during the past 50 years, helped scientists to solve more complex problems that are not feasible to be answered analytically. As a step forward towards addressing the aforementioned questions, we have developed a computational model through which the behavior of the slender filaments can be analyzed [69, 42]. In most scenarios, the slender filaments are interacting with the viscous fluid around them. Therefore, the model should capture both the structural dynamics of the filament and the hydrodynamic interactions between the filament and the surrounding fluid.

Taylor was among the pioneers who studied the hydrodynamic modeling of slender microorganisms at low Reynolds numbers [48]. Since then, many research studies have been conducted on the simulation of microfilaments in viscous fluids at low Reynolds numbers [61]. At low Reynolds numbers or namely Stokes regime where most of the biological microorganisms move, viscous forces are the highly dominant terms and eliminate the effect of inertia in Navier-Stokes equations. This results in sets of linear differential equations usually referred to as Stokes equations or creeping flow equations. Gray and Hancock [40] were also among the pioneers of the classical work in micro swimming kinematics in the 1950s and proposed resistive force theory

(RFT) for flagellar propulsion. RFT [12, 85, 102, 20, 52] establishes a local linear relationship between the hydrodynamic drag force and the velocity of the rod at each cross-section of the filament. They suggested constant normal and tangential drag coefficients that have a logarithmic proportionality to the slenderness ratio of the filament [5, 99, 63]. In this theory, the effect of the shape or curvature of the filament on hydrodynamic drag coefficients is neglected. Moreover, the RFT model does not predict the hydrodynamic interactions with other filaments or rigid objects such as a cargo located at the tail[45], and a rigid wall close to the filament. However, resistive drag coefficients provide an appropriate approximation for the hydrodynamic drag force on a single filament with a high slenderness ratio. Therefore, to determine the hydrodynamic loads on a filament whether in presence of a wall or other neighboring filaments, a higher-order model is required to address the aforementioned shortcomings[31, 55].

More complex mathematical models have been developed to capture the nonlocal hydrodynamic interactions between the flexible filaments and the Stokesian fluid. As of now, boundary element method (BEM)[82, 80, 50, 101, 67, 94, 23], slender body theory (SBT) [83, 84, 81, 43, 20, 4, 63, 45, 12, 53, 61], immersed boundary method (IBM)[23, 105, 105, 54], bead-rod model [22, 21, 65], and regularized stokeslet method (RSM) [94, 23, 16, 17, 18, 19] are among the most popular theories [23]. To accurately determine the fluid velocity field around any arbitrary structure at low Reynolds numbers, BEM can be used. In BEM, the boundary integral equations that are the exact solutions to the Stokes flow need to be solved[59, 73, 83]. This method, however, provides more accuracy but computationally is intensive especially when there are multiple structures with complex geometries [99]. Alternatively, the singularity method —also known as the method of fundamental solutions — is introduced to circumvent the computational difficulties associated with the boundary element method [83, 99]. In this manner, the flow is represented by a line integral or point-wise distribution of appropriate singularity solutions instead of a surface singularity distribution on the structure. Exclusively for a filament with a large but finite length-over-radius ratio, the distribution of stokeslets and potential dipoles along the center-line of the filament is necessary. In essence, SBT is the representation of the flow past the slender filament[83, 84] using the singularity solutions of the Stokes flow.

In this thesis, we employ the SBT method to determine the hydrodynamic interactions of a filament with its surrounding Stokesian fluid. To obtain the dynamics of the filament we introduce our computational rod model and then combined it with SBT. Using the combined fluid-structure interaction model, a lot of interesting questions in engineering and biology that we discussed earlier can be answered.

1.2   Chapters Overview

Chapter 2: we introduce the Stokes equations that govern the fluid motion at very low Reynolds numbers. Since at low Reynolds numbers viscous forces are dominant over the inertial forces, the nonlinear inertial term in the Navier-Stokes equation can be neglected, which results in the remaining sets of linear differential equations known as the Stokes equations. Next, by taking the divergence of the Stokes equation we derive its Green's function referred to as the *Stokeslet*, which is the singularity solution to the Stokes equations in free-space. Similarly, using the Green's function of the Stokes equations we obtain the velocity and pressure field associated with a point force acting on the viscous fluid in an arbitrary direction, and then illustrate them using streamlines and contour plots. The linearity of the Stokes differential equations allows the superposition of the singularity solutions, thus the solution for a flow with multiple point forces of different strengths and directions can be found through the summation of all singularity solutions. However, the flow in proximity of a rigid boundary requires the fluid velocity to vanish on the surface of the rigid structure and therefore the solution to the Stokes flow cannot be determined through the free-space Green's function. We use the method of images inspired by the electrostatics and developed by Blake [8] for the first time, to satisfy the no-slip boundary condition on the surface of the rigid plane wall. In this manner, we employ the higher-order singularity solutions namely *Stokes doublet* and *potential dipole*, which are respectively found through the derivative and the Laplacian of the Stokeslet, and present the Green's function of the Stokes flow in presence of an infinite no-slip plane wall. The velocity and the pressure field subjected to a point force acting in parallel and perpendicular to the plane wall are then demonstrated. Last but not least, we explore the irrotational singularity solutions to the Stokes equations in which the pressure is assumed to be constant. The first singularity solution for the irrotational Stokes flow is named a *Source* and its higher-order solution a *source doublet* or *potential dipole*. It should be noted that the potential dipole and its derivatives can respectively be found through the Laplacian of the Stokeslet and its derivatives. Consequently, the source singularity solutions in presence of a no-slip plane wall are obtained and illustrated.

Chapter 3: In this chapter, we employ the singularity solutions, which are thoroughly discussed in chapter II, to determine the nonlocal hydrodynamic disturbances produced by a slender filament attached to a plane wall while immersed in a viscous fluid. The nonlocal *Slender Body Theory* (SBT) is then introduced to investigate such hydrodynamic interactions between the filament and the fluid. In the SBT, the singularity solutions; Stokeslets and potential dipoles of unknown strengths are distributed along the center-line of the filament. We first determine the singularity strengths which are the same as the hydrodynamic forces on each cross-section of the rod and then through the found force densities we obtain the velocity field around

4

the slender filament. We also discuss the Slender body theory of Cox [20] in which he uses an asymptotic expansion analysis in terms of the slenderness of the rod to obtain an expression for the force density distribution along the center-line of the rod. Next, using the Cox formulation we neglect the higher-order terms to provide a linear relationship between the drag force and the velocity of each cross-section, which is referred to as the *Resistive Force Theory* (RFT) or the *Local Slender Body Theory*. The work of Cox, however, is only applied to a single filament away from any rigid boundary including a no-slip plane wall, and limits our exploration towards the multi-filament or wall-filament studies.

Chapter 4: Now that the hydrodynamic analysis of slender rods is completely discussed in the previous chapters, we would turn our attention towards the dynamics of slender elastic filaments. To capture any small or large deflection of the filament subjected to external forces or moments, we use the Kirchhoff inextensible rod model in which the equations of linear and angular momentum along with the appropriate compatibility equations are written for an infinitesimal cross-section of the rod. The partial differential equations are then combined into a large assembled matrix and solved using the generalized-α method, which is a robust time integrator algorithm that guarantees the stability of the solution. However, at each temporal step, we iterate the solutions within the Newton-Raphson loop until the error to the solution of unknown vectors is sufficiently small. Once the solution at each time step is converged, we employ the method of incremental rotations to obtain the shape of the filament at the corresponding time.

Chapter 5: A survey on the accuracy of the slender body theory (SBT) is conducted. We use a computational fluid dynamic model (CFD) to fully solve the Navier-Stokes equations and obtain the total hydrodynamic drag force on filaments at different slenderness ratios. All the CFD problems are solved using the commercial software, COMSOL Multiphysics v 5.3. In addition to the CFD simulations, we include the local hydrodynamic models that are usually referred to as resistive force theory (RFT). In three different scenarios, the drag force on the rigid filaments is computed: a filament moving in an unbounded domain of fluid away from any rigid boundary, a free-free filament moving in the proximity of a no-slip plane wall, and a fixed-free filament attached to a no-slip wall which is subjected to shear flow. For each scenario, we employ our slender body formulations and illustrate the fluid flow around the filament using the velocity contour plots as well as the velocity streamlines. Then, the comparative graphs are included through which the total hydrodynamic forces versus the slenderness ratios of the filaments are demonstrated.

Chapter 6: An abstract of the work we were supposed to present in the European Nonlinear Dynamics Conference is attached to this chapter of my thesis as a reference for the readers. The conference was supposed to be held in Lyon, France in July 2020

but it was canceled due to the 2019-2020 pandemic. In this abstract, we present the formulations that govern both the dynamics and hydrodynamics of a slender filament that is immersed in a fluid at low Reynold's numbers. The filament becomes unstable and buckles once the non-conservative follower-forces impose external loads to the center-line of the filament. At each time-step, our computational rod model is in charge of capturing the slender rod's deflections/position, linear and angular velocities as well as the internal forces and moments on each cross-section of the rod, which of course depends on the external forces and torques exerted on the filament. In our simulations, the external follower-forces that are directed tangentially to the center-line of the rod at each cross-section are predetermined by the user. Moreover, we employ slender body theory through which we compute the non-uniform hydrodynamic loads imposed from the nearby fluid on each cross-section of the rod. As a result, at each temporal step, the dynamical and hydrodynamical equations are iteratively solved to ensure convergence.

Chapter 7: The conclusion and future work has been discussed.

Before we proceed further, let us introduce the following abbreviations that will be used throughout this thesis:

- CFD (Computational Fluid Dynamics): Results of hydrodynamic loads on a slender cylinder obtained from the COMSOL Multiphysics® v. 5.3 as our CFD solver

- SBT (Slender Body Theory): Results of the hydrodynamic loads on an unbounded cylindrical filament, obtained from our computational model solved via MATLAB® v. R2018b [81, 23]

- W-SBT (Wall-Slender Body Theory): Results of the hydrodynamic loads on a cylindrical filament bounded by a no-slip wall, obtained from our computational model solved via MATLAB® v. R2018b [8, 9, 45]

- RFT (Resistive Force Theory): The leading-order hydrodynamic loads on an unbounded cylindrical filament obtained from SBT formulations [96, 20]

- W-RFT (Wall-Resistive Force Theory): The leading-order hydrodynamic loads on a cylindrical filament bounded by a no-slip wall obtained from W-SBT [12]

Chapter 2

Singularity solutions to the Stokes equations

2.1 Green's Function for Singularly Forced Stokes Flow in Unbounded domain

Navier-Stokes equations are fundamental nonlinear equations that govern the motion of fluid in 3-dimensional space. Here, in equation (2.1) the Navier-Stokes equation along with the continuity equation for an incompressible fluid are given:

$$\rho\frac{\partial \mathbf{u}}{\partial t} + \rho(\mathbf{u} \cdot \boldsymbol{\nabla})\mathbf{u} = -\boldsymbol{\nabla}p + \mu\boldsymbol{\nabla}^2\mathbf{u} \quad , \quad \boldsymbol{\nabla} \cdot \mathbf{u} = 0 \tag{2.1}$$

in which ρ is the fluid density, μ is the fluid viscosity, t is the time, p is the pressure, and $\mathbf{u}$ represents the fluid velocity field. Using non-dimensional parameters V_c and L_c that are the characteristic velocity and length-scale respectively, the non-dimensionalized Navier–Stokes and continuity equation for an incompressible fluid yield:

$$\text{Re}\left(\frac{\partial \mathbf{u}^*}{\partial t^*} + (\mathbf{u}^* \cdot \boldsymbol{\nabla}^*)\mathbf{u}^*\right) = -\boldsymbol{\nabla}^*p^* + \boldsymbol{\nabla}^{*2}\mathbf{u}^* \quad , \quad \boldsymbol{\nabla}^* \cdot \mathbf{u}^* = 0 \tag{2.2}$$

where $*$ denotes the non-demiensionalizad form of each variable and Re is the Reynolds number given by Re $= \rho V_c L_c/\mu$. In equation (2.2) the velocity is scaled by V_c, the pressure p by $\mu V_c/L_c$, time t by L_c/V_c, and the Del operator $\boldsymbol{\nabla}$ by $1/L_c$. At low Reynolds numbers limit where Re $\ll 1$, the term on the left side of equation (2.2) vanishes and the nonlinear Navier-Stokes equations can be reduced to linear Stokes equations, which are solved by a number of methods[99, 66]. Equation (2.3) represents the Stokes equations in the presence of a point force, accompanied by the corresponding boundary conditions, in which $\mathbf{u}^\infty$ and p^∞ are the velocity and the pressure associated with the background flow respectively, $\mathbf{r}$ defines the position of

any point in 3-dimensional space, and $\mathbf{r}_0$ defines the position where the point force is located while both $\mathbf{r}$ and $\mathbf{r}_0$ are taken relative to the inertial reference frame X, Y, Z fixed at the origin (see FIG. 2.1). Mathematically the point force in the Stokes equations can be represented by a 3-dimensional Dirac delta function.
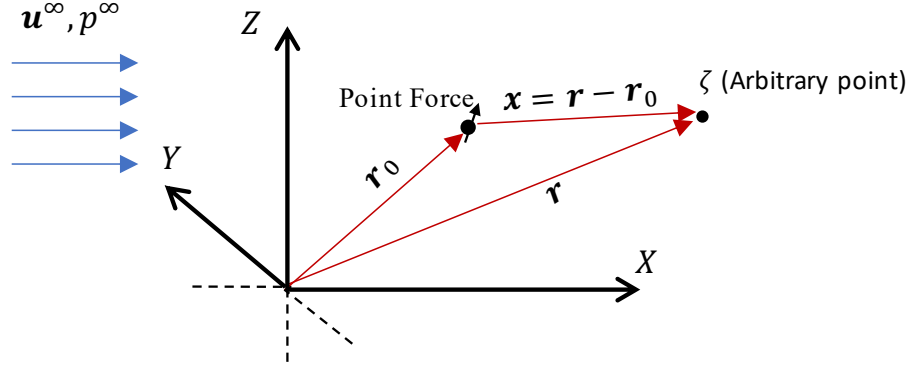
Figure 2.1: Illustration of a point force which is acting on a viscous fluid at $\mathbf{r}_0$, when a background flow is imposed at far-field with the velocity and pressure of $\mathbf{u}^\infty$ and p^∞, respectively. The flow at any point ζ around the point force can be determined using the vector $\mathbf{r} - \mathbf{r}_0$.

$$-\boldsymbol{\nabla}p + \mu\boldsymbol{\nabla}^2\mathbf{u} + \mathbf{f}\delta(\mathbf{r} - \mathbf{r}_0) = \mathbf{0} \quad , \quad \boldsymbol{\nabla} \cdot \mathbf{u} = 0$$
$$\mathbf{u} \to \mathbf{u}^\infty \quad and \quad p \to p_\infty \quad as \quad \mathbf{r} \to \infty$$
(2.3)

Here, δ is the 3-dimensional Dirac delta function with the property $\delta(\mathbf{r} - \mathbf{r}_0) = 0$ when $\mathbf{r} \neq \mathbf{r}_0$. The 3-dimensional Dirac delta function also satisfies $\int_V \delta(\mathbf{r}-\mathbf{r}_0)\ dV = 1$, where V shows any volume that contains the point at which $\mathbf{r} = \mathbf{r}_0$. Correspondingly, $\mathbf{f}\delta(\mathbf{r} - \mathbf{r}_0)$ represents a point force with strength $\mathbf{f}$ acting on the fluid at $\mathbf{r} = \mathbf{r}_0$. The boundary conditions defined for the Stokes flow, enforce the velocity $\mathbf{u}$ and the pressure p to respectively match the velocity and the pressure of the background flow as the position vector $\mathbf{r}$ moves away from the concentrated force which is located at $\mathbf{r}_0$. For instance, if there is no background flow and $\mathbf{u}^\infty$ is zero, the velocity $\mathbf{u}$ should completely vanish at infinity. The Green's function for the Stokes equations in the presence of a singularity, is referred to as the fundamental solution to the Stokes equations or the so-called Stokeslet singularity or the Oseen-Burger Tensor[78]. In the Equation (2.4), $\mathbf{G}(\mathbf{r}, \mathbf{r}_0)$ represents the Green's function for the Stokes equations for a fluid in an unbounded or infinite domain, where $\mathbf{I}$ is the 3-by-3 identity matrix, and $r = |\mathbf{r} - \mathbf{r}_0|$. Higher-order singularity solutions may also be obtained from the

derivative of the fundamental solution that will be discussed later in this chapter.

$$\mathbf{G}(\mathbf{r}, \mathbf{r}_0) = \frac{\mathbf{I}}{r} + \frac{(\mathbf{r} - \mathbf{r}_0) \otimes (\mathbf{r} - \mathbf{r}_0)}{r^3} \tag{2.4}$$

Here, $\otimes$ represents the dyadic products of the vectors, and from now on we drop this notation for any dyadic vector product. Consequently, the fluid velocity field $\mathbf{u}$, which satisfies the aforementioned boundary conditions of the Stokes flow, is given by (2.5):

$$\mathbf{u}(\mathbf{r}) = \mathbf{u}^\infty + \frac{1}{8\pi\mu}\mathbf{G}(\mathbf{r}, \mathbf{r}_0) \cdot \mathbf{f}(\mathbf{r}_0) \tag{2.5}$$

Physically, equation (2.5) represents the fluid velocity field around a point force with strength $\mathbf{f}$ placed at $\mathbf{r}_0$. In (2.5) the velocity of the fluid $\boldsymbol{u}$ can be computed at any observation point $\mathbf{r}$ around the point force except at the source point $\mathbf{r}_0$ where the Stokeslet exhibits singular behaviour. Note that, this is only because of the linearity of the Stokes equations that the solution due to the point force can separately be computed and summed to the solution imposed by the background flow.

(a) velocity contour plot   (b) velocity streamlines   (c) pressure contour plot

Figure 2.2: *Stokeslet*. In the figures above, the fluid velocity and pressure field due to the effect of a point force on a viscous fluid are illustrated. Here, the point force with strength $\mathbf{f} = 8\pi\mu\,(1, 0, 1)$ is placed at the origin of the 3-dimensional euclidean space. 2.1 The contour plot for the logarithm of the velocity magnitude or $\log_{10}(|\mathbf{u}|)$ is shown in which the colours ranging from blue to red correspond to low and high velocity magnitudes, respectively. Note that the velocity behaves singular at $\mathbf{r} = \mathbf{r}_0$ where the point force is located. 2.1 The velocity streamlines are shown in which the black arrow is oriented along the direction of the point force $\mathbf{f}$. 2.1 The pressure associated with the Green's function of the Stokes flow in the presence of a point force is shown. Here, the contours are illustrated for p/μ and the colors ranging from blue to red correspond to the negative and positive pressure, respectively.

9

The pressure at any point associated with the flow in equation (2.3) is given by (2.6):

$$p(\mathbf{r}) = p^\infty + \frac{1}{8\pi}\mathbf{P}(\mathbf{r}, \mathbf{r}_0) \cdot \mathbf{f}(\mathbf{r}_0) \tag{2.6}$$

where the vector $\mathbf{P}$ can be obtained through (2.7):

$$\mathbf{P}(\mathbf{r}, \mathbf{r}_0) = 2\frac{(\mathbf{r} - \mathbf{r}_0)}{r^3} \tag{2.7}$$

For the rest of our study, we restrict ourselves to zero $\mathbf{u}^\infty$ and p^∞ that are associated with the velocity and pressure of the background flow, respectively. It should also be noted that the Stokeslet singularity decays as r^{-1} at far-field, and higher-order singularities that can be constructed from the derivatives of the stokeslet decay faster than the stokeslet singularity. Now, for the purpose of illustration, in FIG. 2.2 the contour plot and the streamlines for the fluid velocity field along with the pressure around a single point force with strength $\mathbf{f} = 8\pi\mu (1, 0, 1)$ are shown. To illustrate the velocity contour plots associated with the singularity solutions more appropriately, the $log_{10}|\mathbf{u}|$ is selected to smoothen the sharp decay of the velocity. For the illustration of each figure in this chapter, –except the schematics figures– the XZ plane is discretized in with 401×401 grid points within the domain $[-1, 1]$ for both the X and the Z directions.

2.2 Derivation of the Stokeslet from the Stokes Equations

In general, the Green's function for the Stokes equations in which a concentrated force acts on the fluid at an specific location, –in this literature $\mathbf{f}\delta(\mathbf{r} - \mathbf{r}_0)$ represents the concentrated force– has been derived through a number of methods [66]. Here, we present the method provided by [83, 73], in which the divergence of the Stokes equations leads us towards the proof of the Green's function given in equation (2.4). we rewrite the Stokes equations which are also given by equation (2.3):

$$-\boldsymbol{\nabla}p + \mu\boldsymbol{\nabla}^2\mathbf{u} + \mathbf{f}\delta(\mathbf{r} - \mathbf{r}_0) = \mathbf{0} \quad , \quad \boldsymbol{\nabla} \cdot \mathbf{u} = \mathbf{0} \tag{2.8}$$

Now, by taking the divergence of the Stokes equation we arrive at:

$$-\boldsymbol{\nabla} \cdot \boldsymbol{\nabla}p + \mu\boldsymbol{\nabla} \cdot \boldsymbol{\nabla}^2\mathbf{u} + \boldsymbol{\nabla} \cdot (\mathbf{f}\delta(\mathbf{r} - \mathbf{r}_0)) = 0 \tag{2.9}$$

Considering the commutative property of the Laplacian and the divergence operators which reminds $\boldsymbol{\nabla} \cdot (\boldsymbol{\nabla}^2\mathbf{u}) = \boldsymbol{\nabla}^2(\boldsymbol{\nabla} \cdot \mathbf{u})$, and using the continuity equation $\boldsymbol{\nabla} \cdot \mathbf{u} = \mathbf{0}$ we obtain the following equation:

$$\boldsymbol{\nabla}^2p - \mathbf{f} \cdot \boldsymbol{\nabla}\delta(\mathbf{r} - \mathbf{r}_0) = 0 \tag{2.10}$$

10

Now, let us define the scalar functions $\mathbf{K}$ and $\mathbf{H}$ such that they satisfy the following equations, respectively:

$$\boldsymbol{\nabla}^2\mathbf{K} = \delta(\mathbf{r} - \mathbf{r}_0) \quad , \quad \mathbf{K} = \boldsymbol{\nabla}^2\mathbf{H} \tag{2.11}$$

Therefore, equation (2.10) can be rewritten in terms of $\mathbf{K}$ as:

$$\boldsymbol{\nabla}^2 p - \mathbf{f} \cdot \boldsymbol{\nabla}\boldsymbol{\nabla}^2\mathbf{K} = 0 \tag{2.12}$$

that results in an expression for the pressure:

$$p = \mathbf{f} \cdot \boldsymbol{\nabla}\mathbf{K} \tag{2.13}$$

In order to obtain an expression for the velocity $\mathbf{u}$, we need to determine the gradient of the pressure from the equation (2.13), which yields:

$$\boldsymbol{\nabla} p = \mathbf{f} \cdot \boldsymbol{\nabla}(\boldsymbol{\nabla}\mathbf{K}) \tag{2.14}$$

and substitute (2.14) in the Stokes equation given by (2.8). After rearranging the new equation, and letting $\mathbf{I}$ denote the identity matrix, we obtain:

$$\boldsymbol{\nabla}^2\mathbf{u} = \frac{1}{\mu}\mathbf{f} \cdot (\boldsymbol{\nabla}\boldsymbol{\nabla} - \mathbf{I}\boldsymbol{\nabla}^2)\mathbf{K} \tag{2.15}$$

Now, defining $\mathbf{K}$ in terms of the Laplacian of $\mathbf{H}$ as is shown in (2.11) we acquire an expression for the velocity field $\mathbf{u}$ which is:

$$\mathbf{u} = \frac{1}{\mu}\mathbf{f} \cdot (\boldsymbol{\nabla}\boldsymbol{\nabla} - \mathbf{I}\boldsymbol{\nabla}^2)\mathbf{H} \tag{2.16}$$

We recall that the harmonic expression on the left side of (2.11) represents the Poisson's equation and $\mathbf{K}$ is the fundamental solution of the Poisson's equation, which is given as:

$$\mathbf{K} = \frac{-1}{4\pi r} \tag{2.17}$$

where $r = |\mathbf{r} - \mathbf{r}_0|$. In a similar manner, $\mathbf{H}$ can be constructed from $\mathbf{K}$ using the relation defined on the right side of (2.11), which yields:

$$\mathbf{H} = \frac{-r}{8\pi} \tag{2.18}$$

As a result, by substituting (2.18) into (2.16) we obtain the velocity field at any point around the concentrated force, which is represented in Einstein notation as:

$$u_i(\mathbf{r}) = \frac{1}{8\pi\mu}G_{ij}(\mathbf{r} - \mathbf{r}_0)f_j \tag{2.19}$$

11
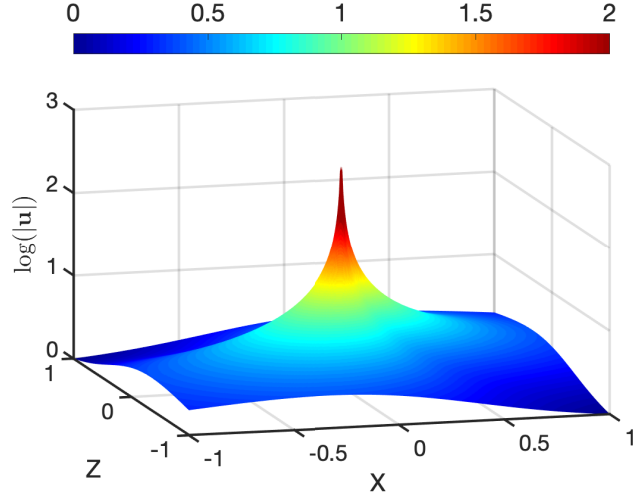
Figure 2.3: A 3D surface plot for the velocity field attributed to the equation (2.19) or (2.5) is illustrated. It is shown that the velocity behaves singular at its pole $\mathbf{r}_0$, but remains regular at the other points around the singularity. A similar plot but in 2D can be found in FIG. 2.2 as well.

where $\mathbf{G}$ is called the *Stokeslet* and given by:

$$G_{ij}(\mathbf{x}) = \frac{\delta_{ij}}{r} + \frac{x_i x_j}{r^3} \tag{2.20}$$

in which δ_{ij} represents the Kronecker delta, $\mathbf{x} = \mathbf{r} - \mathbf{r}_0$, and $r = |\mathbf{r} - \mathbf{r}_0| = \sqrt{x_1^2 + x_2^2 + x_3^2}$. Both the velocity and the Green's function in (2.19) and (2.20) are also given in vectorial and tensorial representations by equations (2.5) and (2.4), respectively.

2.3 Multiple Point Forces in Stokes Flow

In the Stokes equations, it is convenient to consider a point force as the force exerted by an infinitesimal particle that is immersed in a viscous fluid. When many small particles approach each other, the flow field around one particle will be affected by the other particles. Similarly, the flow field in proximity of a point force cannot be obtained through the equation (2.5) in which the Green's function for a single point force has been used. However, the linearity of the Stokes equations allows the superposition of singularity solutions. Thus, to obtain the solution of the Stokes equations due to the presence of n point forces with strengths $\mathbf{f}_1$, $\mathbf{f}_2$, ..., $\mathbf{f}_n$ in a viscous fluid, the solutions for the velocity and the pressure obtained by equations

(2.5) and (2.6) due to each singularity, are only required to be summed with the rest of singularity solutions so that the velocity and the pressure field affected by multiple singularities can readily be determined. In this section, we investigate the effect of two and four point forces on the velocity field and illustrate the corresponding flow fields using streamlines and contour plots. Now, let the two point forces with strength $\mathbf{f}_1$ and $\mathbf{f}_2$ act on the viscous flow at two different locations $\mathbf{r}_{0,1}$ and $\mathbf{r}_{0,2}$. In this limit, to obtain the velocity field around the singularities, the equation (2.5) can be modified into equation (2.21):

$$\mathbf{u}(\mathbf{r}) = \frac{1}{8\pi\mu} \sum_{j=1}^{n} \mathbf{G}(\mathbf{r}, \mathbf{r}_{0,j}) \cdot \mathbf{f}_j \tag{2.21}$$

with $n = 2$. Similarly, in order to obtain the pressure field, the equation (2.6) can be modified into the equation (2.22):

$$p(\mathbf{r}) = \frac{1}{8\pi} \sum_{j=1}^{n} \mathbf{P}(\mathbf{r}, \mathbf{r}_{0,j}) \cdot \mathbf{f}_j \tag{2.22}$$

In FIG. 2.5 the flow fields due to the presence of two point forces with same magnitude but opposite directions are illustrated. In the first example, $\mathbf{f}_1$ is aligned with the $\mathbf{f}_2$ and in the second example $\mathbf{f}_1$ is taken to be in parallel with $\mathbf{f}_2$.

(a) velocity contour plot   (b) velocity streamlines   (c) pressure contour plot

(d) velocity contour plot   (e) velocity streamlines   (f) pressure contour plot
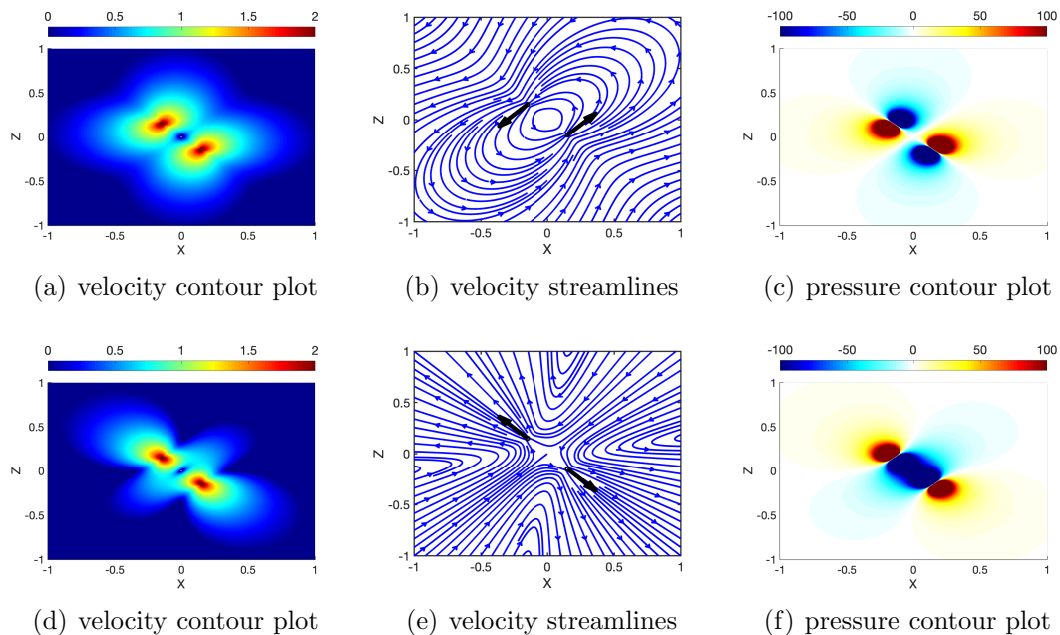
Figure 2.4: In the figures above, the fluid velocity and pressure field due to two point forces acting on a viscous fluid are illustrated. In the first row, one of the point forces with $\mathbf{f_1} = 8\pi\mu(-1, 0, -1)$ is placed at $\mathbf{r}_{0,1} = (-d, 0, d)$ and the second point force with $\mathbf{f_2} = 8\pi\mu(1, 0, 1)$ which acts in parallel but on the opposite direction of $\mathbf{f}_1$, is placed at $\mathbf{r}_{0,2} = (d, 0, -d)$ where d is chosen to be 0.15 for this simulation. In the second row, the orientation of the point forces are chosen to be aligned but in opposite with each other such that $\mathbf{f_1} = 8\pi\mu(-1, 0, 1)$ and $\mathbf{f_2} = 8\pi\mu(1, 0, -1)$. 2.3,2.3 The contour plot for the logarithm of the velocity magnitude or $\log_{10}(|\mathbf{u}|)$ is shown in which the colours ranging from blue to red correspond to low and high velocity magnitudes, respectively. Note that the velocity behaves singular at $\mathbf{r}_{01}$ and $\mathbf{r}_{02}$ where the point forces are located. 2.3,2.3 The velocity streamlines are shown in which the black arrows are oriented along the direction of each point force $\mathbf{f_1}$ and $\mathbf{f_2}$. 2.3,2.3 The pressure associated with the Green's function of the Stokes flow in the presence of two point forces are shown. Here, the contours are illustrated for p/μ and the colors ranging from blue to red correspond to the negative and positive pressure, respectively.

14

(a) Velocity contour plot   (b) Velocity streamlines   (c) Pressure contour plot

(d) Velocity contour plot   (e) Velocity streamlines   (f) Pressure contour plot
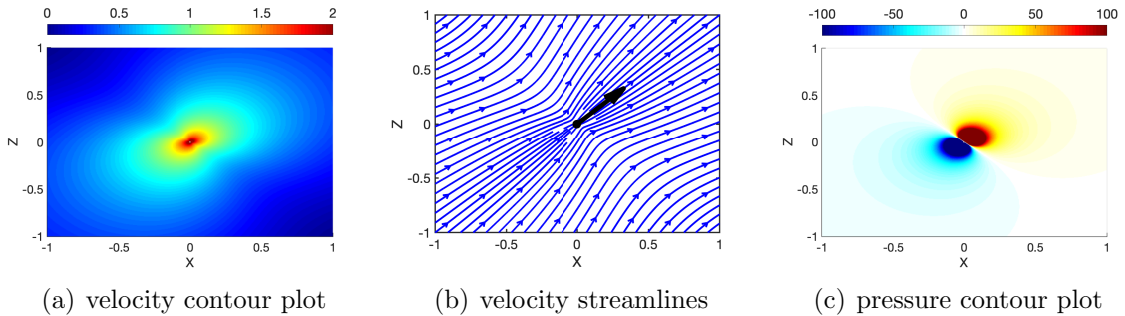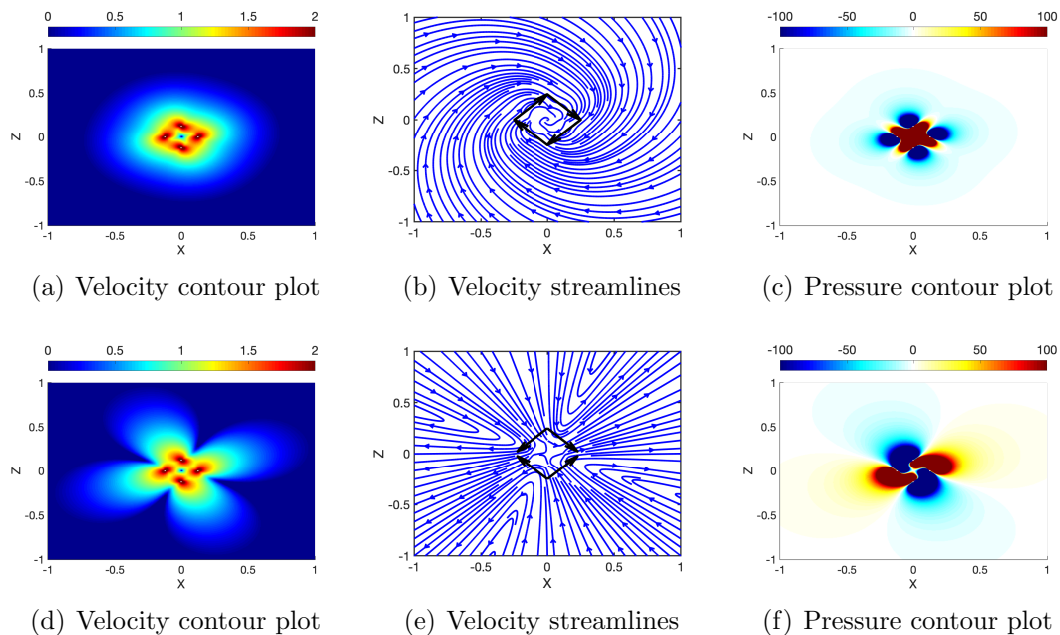
Figure 2.5: In the figures above, the fluid velocity and the pressure field due to four point forces acting on a viscous fluid are illustrated. The first row is attributed to the point forces with strengths $\mathbf{f_1} = 8\pi\mu(1,0,1)$, $\mathbf{f_2} = 8\pi\mu(1,0,-1)$, $\mathbf{f_3} = 8\pi\mu(-1,0,-1)$, $\mathbf{f_4} = 8\pi\mu(-1,0,1)$ are positioned at $\mathbf{r}_{01} = (-d,0,0)$, $\mathbf{r}_{02} = (0,d,0)$, $\mathbf{r}_{03} = (d,0,0)$, $\mathbf{r}_{04} = (0,-d,0)$, respectively, where d is chosen to be 0.25 for both simulations in the first and the second row. The second row is attributed to the point forces with strengths $\mathbf{f_1} = 8\pi\mu(-1,0,-1)$, $\mathbf{f_2} = 8\pi\mu(1,0,-1)$, $\mathbf{f_3} = 8\pi\mu(1,0,1)$, $\mathbf{f_4} = 8\pi\mu(-1,0,1)$ that are located at the same locations in the figures of the first row, respectively. 2.3,2.3The contour plot for the logarithm of the velocity magnitude or $\log_{10}(|\mathbf{u}|)$ is shown in which the colours ranging from blue to red correspond to the low and high velocity magnitudes, respectively. 2.3,2.3 The velocity streamlines are shown in which the black arrows are oriented along the direction of each one of the point forces. 2.3,2.3 The pressure associated with the Green's function of the Stokes flow in the presence of four point forces are shown. Here, the contours are illustrated for p/μ and the colors ranging from blue to red correspond to the negative and positive pressure, respectively.

2.4 Singularly Forced Stokes Flow Bounded by an Infinite No-slip Plane Wall

In the previous sections, we first introduced the Green's function for the Stokes equations in presence of a point force acting on the fluid at the origin of the reference frame. Then taking advantage of the linearity of the Stokes equations, we showed the singularity solutions for multiple point forces acting on the Stokes flow using the equation (2.21) and (2.22) associated with the velocity and pressure fields, respectively. The Green's function in equation (2.4) is only a solution to the Stokes equations when no rigid boundary affects the flow. The presence of a rigid boundary requires the Stokes equations to satisfy the no-slip boundary condition on the surface of the rigid body. Therefore, Green's function (2.4) is not the correct choice for the Stokes flow bounded by a rigid body and a different Green's function is required. In this section, we consider the semi-infinite Stokes flow in which the flow has been bounded by a rigid plane wall at one side. Then, we assume that a point force with strength $\mathbf{f}$ and at distance h from the plane wall acts on the fluid. The appropriate form of the Green's function that satisfies the no-slip boundary condition on the surface of the rigid wall is given by Blake[8]. Blake's method is similar to the method of images in electrostatics and uses image systems (see FIG. 2.6) to obtain the solution for the velocity and the pressure around a point force consistent with the boundary condition on an infinite plane wall. The appropriate form of Green's function that satisfies the no-slip boundary condition on the surface of the wall is obtained through a combination of Stokeslet, image Stokeslet, image potential dipole, and image Stokeslet doublet. The potential dipole is an irrotational source singularity which can be obtained using the laplacian of the Stokeslet, and the Stokes doublet is the higher-order solution for the Stokes equations and is simply obtained from the derivative of the Stokeslet with respect to its pole $\mathbf{r}_0$. The Green's function in equation (2.23) for the semi-infinite flow bounded by a rigid plane wall is given by [83, 35, 8] but here, the expression provided by Pozrikidis[83] is selected (please note that for the sake of consistency in this chapter, equations provided by Pozrikidis are modified based on our own reference frame and then the corresponding formulations are presented. However, for the wall-corrected Green's function of the Stokes equations, we have directly derived and used the original formulations given by Blake that can be found in [8, 9]):
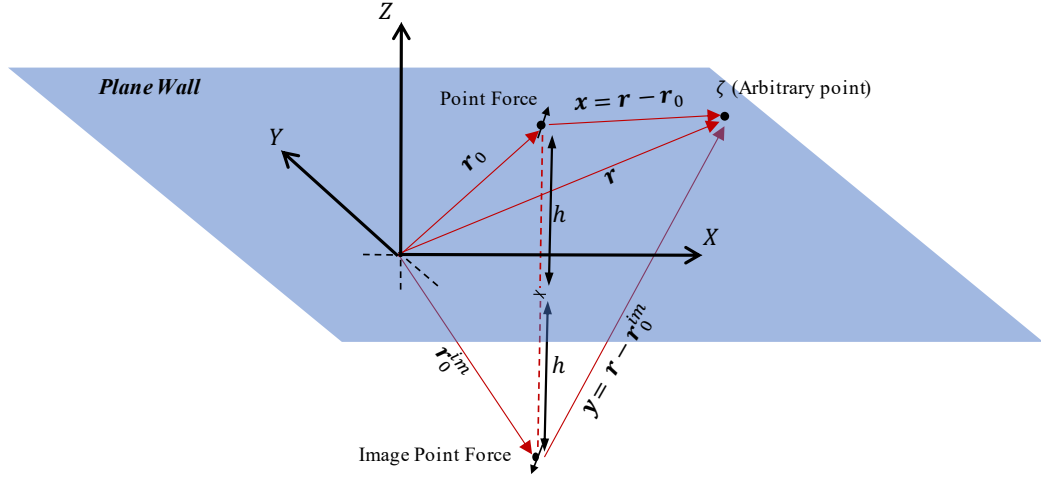
Figure 2.6: The position of the point force and its image with respect to the rigid plane wall in 3-dimensional space are illustrated. It is shown that $\mathbf{r}_0$ and $\mathbf{r}_0^{im}$ are the vectors that respectively mark the position of the point force and its image positioned at distance h from the rigid wall, and vector $\mathbf{r}$ maps the position of any arbitrary point ζ in 3-dimensional space.

$$\mathbf{G}^w(\mathbf{r}, \mathbf{r}_0) = \mathbf{G}(\mathbf{r}, \mathbf{r}_0) - \mathbf{G}(\mathbf{r}, \mathbf{r}_0^{im}) - 2h\mathbf{G}^{SD}(\mathbf{r}, \mathbf{r}_0^{im}) + 2h^2\mathbf{G}^{PD}(\mathbf{r}, \mathbf{r}_0^{im}) \qquad (2.23)$$

where $\mathbf{G}(\mathbf{r}, \mathbf{r}_0)$ is the Stokeslet and $\mathbf{G}(\mathbf{r}, \mathbf{r}_0^{im})$ is the image of the Stokeslet with respect to the rigid wall, which is located at $Z = 0$. The $\mathbf{G}^{SD}$ and $\mathbf{G}^{PD}$ are associated with the Stokeslet doublet and the potential dipole respectively, and for any vector $\mathbf{y} = (y_1, y_2, y_3)$ where $\mathbf{y} = \mathbf{r} - \mathbf{r}_0^{im}$ and $R = |\mathbf{r} - \mathbf{r}_0^{im}| = \sqrt{y_1^2 + y_2^2 + y_3^2}$ they are given in Einstein notation by (2.24) and (2.25):

$$\mathbf{G}^{SD}(\mathbf{r}, \mathbf{r}_0^{im}) = G_{ij}^{SD}(\mathbf{y}) = y_3 G_{ij}^{PD}(\mathbf{y}) \pm \left(\frac{\delta_{j3}y_i}{R^3} - 3\frac{\delta_{i3}y_j}{R^5} \right) \qquad (2.24)$$

$$\mathbf{G}^{PD}(\mathbf{r}, \mathbf{r}_0^{im}) = G_{ij}^{PD}(\mathbf{y}) = \pm \left(\frac{\delta_{ij}}{R^3} - 3\frac{y_iy_j}{R^5} \right) \qquad (2.25)$$

with negative sign for $j = 3$ which is associated with the Z direction, and positive sign for $j = 1, 2$ corresponding to the X and Y directions where δ_{ij} represents the Kronecker delta. Note that the singularity is located at $\mathbf{r_0} = (r_{0_1}, r_{0_2}, h)$, remembering that h represents the distance from the plane wall located at $Z = 0$ so that the image singularity with respect to the wall should be found at $\mathbf{r}_0^{im} = (r_{0_1}, r_{0_2}, -h)$. The pressure corresponding to the Green's function (2.23) is expressed in (2.26):

17

(a) Velocity contour plots   (b) Velocity Streamlines   (c) Pressure contour plots

(d) Velocity contour plots   (e) Velocity Streamlines   (f) Pressure contour plots
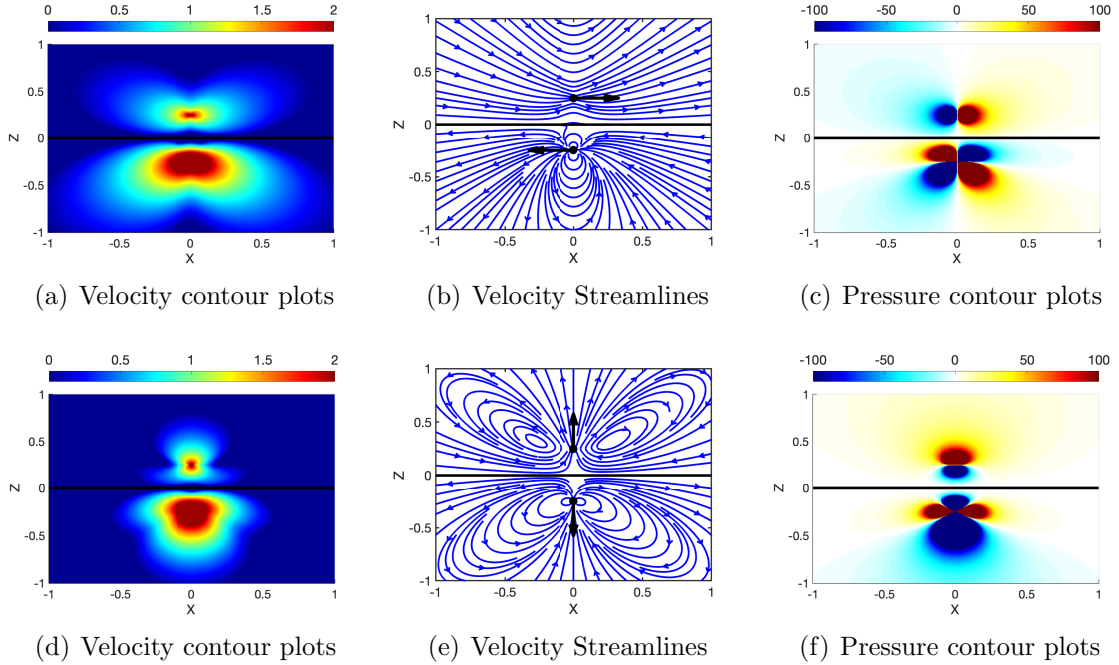
Figure 2.7: *Stokeslet in the presence of a no-slip plane wall.* The fluid velocity and the pressure field due to a point force acting on a viscous fluid that is bounded by a rigid plane wall, are illustrated. The solid line in the middle of each figure represents the rigid wall and the bottom part of the wall represents the contribution of image singularities to the Stokeslet singularity located on the top of the wall. In the first row, the point force with $\mathbf{f} = 8\pi\mu(1,0,0)$ is placed at $\mathbf{r}_0 = (0,0,d)$ where d is chosen to be 0.25 for this simulation, and the image which is placed at $\mathbf{r}_0^{im} = (0,0,-d)$ is oriented in parallel to the wall with strength $-\mathbf{f}$. In the second row, only the point force acts perpendicularly to the plane wall with $\mathbf{f} = 8\pi\mu(0,0,1)$.2.4,2.4 The contour plot for the logarithm of the velocity magnitude or $\log_{10}(|\mathbf{u}|)$ is shown in which the colours ranging from blue to red correspond to the low and high velocity magnitudes, respectively. 2.4,2.4 The velocity streamlines are shown in which the black arrows are oriented along the direction of the point force and its image, respectively. 2.4,2.4 The pressure associated with the Green's function of the Stokes flow in the presence of four point forces are shown. Here, the contours are illustrated for p/μ and the colors ranging from blue to red correspond to the negative and positive pressure, respectively.

$$\mathbf{P}^w(\mathbf{r}, \mathbf{r}_0) = \mathbf{P}(\mathbf{r}, \mathbf{r}_0) - \mathbf{P}(\mathbf{r}, \mathbf{r}_0^{im}) - 2h\mathbf{P}^{SD}(\mathbf{r}, \mathbf{r}_0^{im}) \tag{2.26}$$

where $\mathbf{P}^{SD}$ is:

$$\mathbf{P}^{SD}(\mathbf{r}, \mathbf{r}_0^{im}) = P_i^{SD}(\mathbf{y}) = \pm 2 \left(\frac{\delta_{i3}}{R^3} - 3\frac{y_3 y_i}{R^5} \right) \tag{2.27}$$

again with negative sign for $i = 3$ which is associated with the Z direction, and positive sign for $i = 1, 2$ corresponding to the X and Y direction of the Cartesian coordinate system. We end up this section with the illustration of the velocity and pressure field for a point force which acts on the viscous flow in parallel, and perpendicular to the rigid plane wall.

2.5 Irrotational Singularities of Unbounded Stokes Flow

In the proceeding sections, we solved the Stokes equations in the presence of a point force while the pressure was assumed to be non-constant throughout the domain in which the fluid flow exists. In this section, we turn our attention towards the potential theory and identify the source singularity solutions for the Stokes flow. We begin with selecting the simplest choice for the pressure that is $p = c_0$ in which c_0 is a constant[83, 84]. Then, by substituting $\boldsymbol{\nabla} p = 0$ in the Stokes equation, we will obtain a harmonic equation for the velocity $\boldsymbol{\nabla}^2 \mathbf{u} = \mathbf{0}$. Now, let a scalar function ϕ, which is referred to as the *potential function*, be defined such that the velocity field can be determined through:

$$\mathbf{u} = \boldsymbol{\nabla}\phi \tag{2.28}$$

Using the equation (2.28), the irrotationality of the potential flow is guaranteed since the curl of the gradient of any scalar function is zero, which means:

$$\boldsymbol{\nabla} \times \mathbf{u} = \boldsymbol{\nabla} \times \boldsymbol{\nabla}\phi = \mathbf{0}. \tag{2.29}$$

Taking the particular choice of $\phi = -1/4\pi r$ for the potential function in which $r = |\mathbf{r} - \mathbf{r}_0|$, the velocity field due to a point source that is also illustrated in FIG. 2.8 can be identified through

$$\mathbf{u} = \frac{c}{4\pi}\mathbf{S}(\mathbf{r}, \mathbf{r}_0) \tag{2.30}$$

in which c represents a constant and the point source $\mathbf{S}$ centered at $\mathbf{r}_0$, is given by:

$$\mathbf{S}(\mathbf{r}, \mathbf{r}_0) = \frac{\mathbf{r} - \mathbf{r}_0}{r^3} \tag{2.31}$$

19

(a) Velocity contour plots

(b) Velocity Streamlines
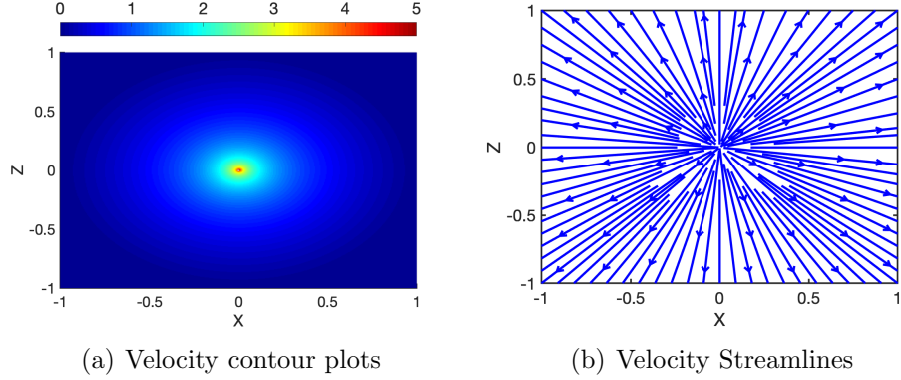
Figure 2.8: *Point Source.* In the figures above, the fluid velocity field due to the effect of a point source on a viscous fluid are illustrated. Here, the point source with strength $c = 4\pi$ is placed at the origin of the 3-dimensional euclidean space. 2.5 The contour plot for the logarithm of the velocity magnitude or $\log_{10}(|\mathbf{u}|)$ is shown in which the colours ranging from blue to red correspond to the low and high velocity magnitudes, respectively. Note that the velocity behaves singular at $\mathbf{r} = \mathbf{r}_0 = \mathbf{0}$ where the point source is located. 2.5 The velocity streamlines are illustrated.

Higher-order source singularity solutions namely, point source dipole, point source quadruple, point source octuple —alternatively in some literature potential dipole, potential quadruple, potential octuple are used— are constructed from the derivatives of the the point source with respect to the $\mathbf{r}_0$. Since, we have confined our study to the use of potential dipole, which its application to slender body hydrodynamics will be discussed in the next chapter, the reader is referred to [83, 9, 95] for the complete expression of the higher-order singularities. The first derivative of the point source therefore provides an expression for the potential dipole, that may be written as:

$$\mathbf{D}(\mathbf{r}, \mathbf{r}_0) = \frac{\partial \mathbf{S}(\mathbf{r}, \mathbf{r}_0)}{\partial \mathbf{r}_0} = -\frac{\mathbf{I}}{r^3} + 3\frac{(\mathbf{r} - \mathbf{r}_0)(\mathbf{r} - \mathbf{r}_0)}{r^5} \tag{2.32}$$

and the flow due to the potential dipole is given by

$$\mathbf{u} = \frac{1}{4\pi}\mathbf{D}(\mathbf{r}, \mathbf{r}_0) \cdot \mathbf{d}(\mathbf{r}_0) \tag{2.33}$$

where $\mathbf{d}$ represents a constant vector. Alternatively, it can be shown that the potential dipole can be found by from the Laplacian of the Stokeslet multiplied by $-1/2$, which means $\mathbf{D} = -\frac{1}{2}\nabla^2\mathbf{G}$. In a similar manner, higher-order source singularities can be obtained from the Laplacian of the derivatives of the point force singularities of the Stokes equations. In FIG. 2.9 the flow due to a potential dipole of strength $\mathbf{d} = 4\pi(1, 0, 1)$ is illustrated. However, the aforementioned source singularities are

20

only attributed to a viscous flow in which the fluid is not bounded by any rigid boundary. The presence of a rigid boundary in the flow requires the fluid velocity to vanish on the surface of the boundary, therefore, the source singularity solutions of the Stokes flow in unbounded domain are not correct choices in representation of the velocity. In the next section, using the image system we explore the source singularity solutions that satisfy the no-slip boundary condition on the surface of the plane wall.

(a) Velocity contour plots (b) Velocity Streamlines
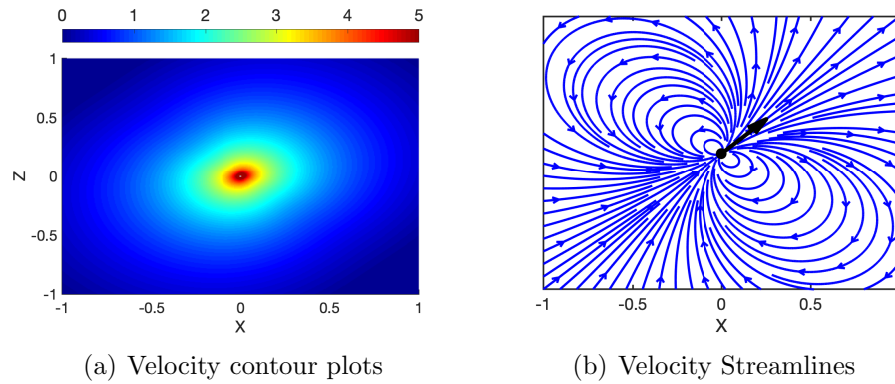
Figure 2.9: *Potential Dipole.* Here, the fluid velocity due to the effect of the potential dipole singularity –also referred to as point source doublet– is illustrated using contour plots and streamlines. Note that the point source with strength $\mathbf{d} = 4\pi(1, 0, 1)$ is placed at the origin of the 3-dimensional euclidean space. 2.5 The contour plot for the logarithm of the velocity magnitude or $\log_{10}(|\mathbf{u}|)$ is shown in which the colours ranging from blue to red correspond to the low and high velocity magnitudes, respectively. Remember that the velocity behaves singular at $\mathbf{r} = \mathbf{r}_0 = \mathbf{0}$ where the potential dipole is located.2.5 The velocity streamlines are illustrated.

2.6 Irrotational Singularities of bounded Stokes Flow

The source singularities of the Stokes flow within a domain where the fluid is bounded by a rigid plane wall, not only exhibit vanishing velocity at infinity but also are required to satisfy the no-slip boundary condition on the surface of the wall. Similar to the point force singularities in the presence of a no-slip plane wall that is discussed in section 2.4, [9] agian exploited the method of images to distribute the same and higher-order singularities at the point where the image of the main source is positioned, to satisfy the no-slip boundary condition on the surface of the plane wall. Consequently,

the velocity for a point source close to a wall is obtained through (2.34):

$$\mathbf{u} = \frac{c}{4\pi}\mathbf{S}^w(\mathbf{r}, \mathbf{r}_0) \tag{2.34}$$

in which the decomposition of the $\mathbf{S}^w$ is represented by [83] as:

$$S_i^w(\mathbf{r}, \mathbf{r}_0) = S_i(\mathbf{r}, \mathbf{r}_0) - S_i(\mathbf{r}, \mathbf{r}_0^{im}) + 2G_{i33}^D(\mathbf{r}, \mathbf{r}_0^{im}) - 2hD_{i3}(\mathbf{r}, \mathbf{r}_0^{im}) \tag{2.35}$$

where the last two singularities respectively the Stokeslet doublet $\mathbf{G}^D$ and the potential dipole $\mathbf{D}$ are oriented perpendicular to the wall. The stokeslet doublet $\mathbf{G}^D(\mathbf{r}, \mathbf{r}_0^{im})$ is written as:

$$G_{ijl}^D = \frac{\delta_{ij}y_l - \delta_{il}y_j - \delta_{jl}y_i}{R^3} + 3\frac{y_iy_jy_l}{R^5} \tag{2.36}$$

however, the $\mathbf{S}^w$ is also directly obtained and given as:

$$S_i^w = \frac{x_i}{r^3} + \frac{y_i}{R^3} + 2y_i\left(-\frac{1}{R^3} + 3\frac{y_3^2}{R^5}\right) - 2h\left(-\frac{\delta_{i3}}{R^3} + 3\frac{y_iy_3}{R^5}\right) \tag{2.37}$$

considering the definition for $\mathbf{x} = (x_1, x_2, x_3) = \mathbf{r} - \mathbf{r}_0$ where $r = |\mathbf{r} - \mathbf{r}_0| = \sqrt{x_1^2 + x_2^2 + x_3^2}$, and $\mathbf{y} = (y_1, y_2, y_3) = \mathbf{r} - \mathbf{r}_0^{im}$ where $R = |\mathbf{r} - \mathbf{r}_0^{im}| = \sqrt{y_1^2 + y_2^2 + y_3^2}$, along with δ_{ij} that represents the Kronecker delta. In FIG. 2.10 the flow due to a point source in the presence of a rigid wall is illustrated.

To obtain the potential dipole above a plane wall, the point source above a wall $\mathbf{S}^w(\mathbf{r}, \mathbf{r}_0)$ should be derived with respect to its pole $\mathbf{r}_0$. The expression for the potential dipole that satisfies the no-slip boundary condition on the surface of the wall is given by [9, 83] as:

$$D_{ij}^w(\mathbf{r}, \mathbf{r}_0) = D_{ij}(\mathbf{r}, \mathbf{r}_0) \pm \left(D_{ij}(\mathbf{r}, \mathbf{r}_0^{im}) + 2G_{i33j}^Q(\mathbf{r}, \mathbf{r}_0^{im}) - 2hQ_{i3j}(\mathbf{r}, \mathbf{r}_0^{im})\right) - 2\delta_{j3}\,D_{i3}(\mathbf{r}, \mathbf{r}_0^{im}) \tag{2.38}$$

with the negative sign for $j = 3$ and positive sign for $j = 1, 2$. In (2.38) the $\mathbf{G}^Q$ is referred to the Stokeslet quadruple which is a tensor of rank four and is obtained by two times deriving the Stokeslet with respect to its pole at $\mathbf{r}_0$. Here, with the same definition for $\mathbf{x}$ and $\mathbf{y}$ as explained earlier, the Stokeslet quadruple is given by [83] as:

$$\begin{aligned}
G_{ijlm}^Q = {}&\frac{1}{R^3}\left(\delta_{il}\delta_{jm} + \delta_{im}\delta_{jl} - \delta_{ij}\delta_{lm}\right)\\
&- \frac{3}{R^5}\left(\delta_{lm}y_iy_j + \delta_{jm}y_iy_l + \delta_{jl}y_iy_m + \delta_{im}y_jy_l + \delta_{il}y_jy_m - \delta_{ij}y_ly_m\right) + 15\frac{y_iy_jy_ly_m}{R^7}
\end{aligned}$$
$$\tag{2.39}$$

(a) Velocity contour plots

(b) Velocity Streamlines
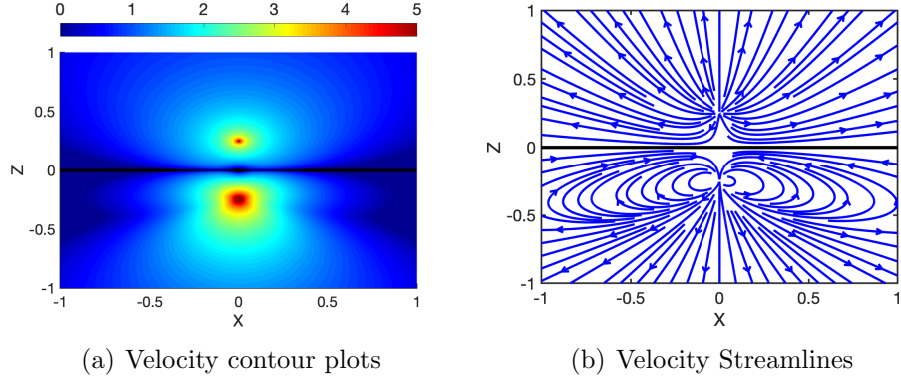
Figure 2.10: *Point Source in the presence of a no-slip plane wall.* In the figures above, the contour plot and streamlines of the fluid velocity due to a point source above the rigid plane wall, are illustrated. Here, the point source with strength $c = 4\pi$ is placed at $\mathbf{r}_0 = (0, 0, d)$ where d is chosen to be 0.25. 2.6 The contour plot for the logarithm of the velocity magnitude or $\log_{10}(|\mathbf{u}|)$ is shown in which the colours ranging from blue to red correspond to the low and high velocity magnitudes, respectively. Note that the velocity behaves singular at $\mathbf{r} = \mathbf{r}_0$ where the point source is located. 2.6 The velocity streamlines are illustrated.

Also the term $\mathbf{Q}(\mathbf{r}, \mathbf{r}_0^{im})$ in equation (2.38) is called the potential quadruple, which can be obtained from the deriative of the potential dipole with respect to the pole $\mathbf{r}_0$. The expression for the potential quadruple is given by [83] as:

$$Q_{ijl} = -3\frac{\delta_{ij}y_l + \delta_{il}y_j + \delta_{jl}y_i}{R^5} + 15\frac{y_i y_j y_l}{R^7} \tag{2.40}$$

Consequently, the velocity due to a potential dipole above a plane wall with strength $\mathbf{d}$ is written as:

$$\mathbf{u} = \frac{1}{4\pi}\mathbf{D}^w(\mathbf{r}, \mathbf{r}_0) \cdot \mathbf{d}(\mathbf{r}_0) \tag{2.41}$$

In this chapter, we investigated the singularity solutions for the Stokes equations including the Stokeslet, Source, source doublet (or potential dipole) both in free-space and above a no-slip plane wall. In the next chapter, we introduce the *singularity method* and *slender body theory* by which we explore how singularity solutions of the Stokes flow are employed to determine the hydrodynamic drag load on slender filaments.

f

(a) Velocity contour plots

(b) Velocity Streamlines

(c) Velocity contour plots

(d) Velocity Streamlines
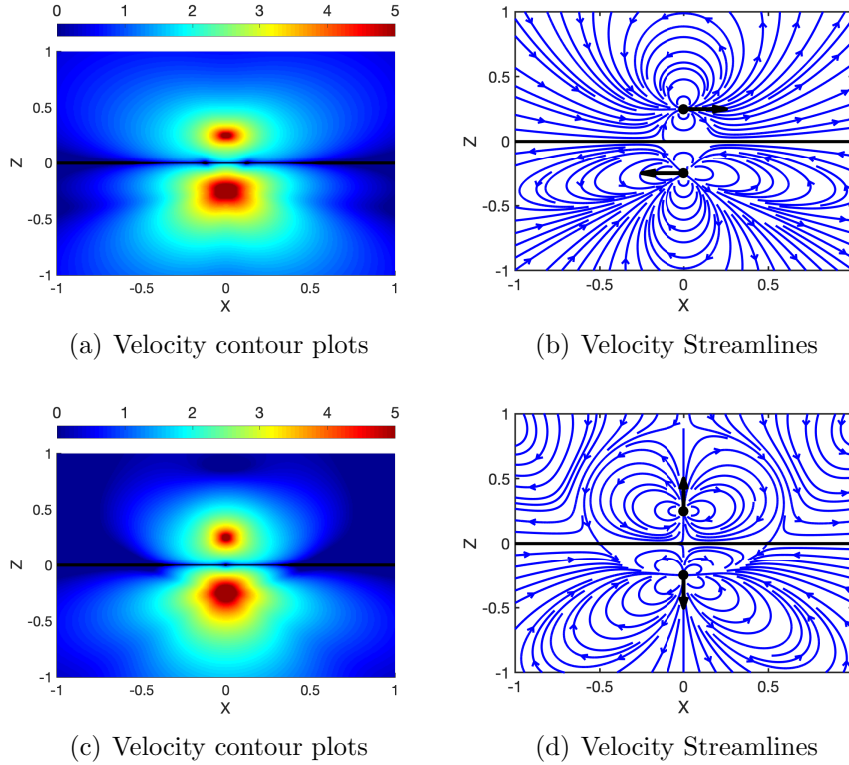
Figure 2.11: *Potential dipole in the presence of a no-slip plane wall.* The velocity contours and streamlines due to a potential dipole acting on a viscous fluid close to a rigid plane wall, are illustrated. The solid line in the middle of each figure represents the rigid wall and the bottom part of the wall represents the contribution of image singularities to the main source singularity located on the top of the wall. In the first row, the potential dipole strength with $\mathbf{d} = 4\pi(1, 0, 0)$ is placed at $\mathbf{r}_0 = (0, 0, d)$ where d is chosen to be 0.25 for this simulation, and the image, which is placed at $\mathbf{r}_0^{im} = (0, 0, -d)$, is oriented in parallel to the plane wall with strength $-\mathbf{d}$. In the second row, the potential dipole acts perpendicular to the plane wall with $\mathbf{d} = 4\pi(0, 0, 1)$.2.6,2.6 The contour plot for the logarithm of the velocity magnitude or $\log_{10}(|\mathbf{u}|)$ is shown in which the colours ranging from blue to red correspond to the low and high velocity magnitudes, respectively. 2.6,2.6 The velocity streamlines are shown in which the black arrows are oriented along the direction of the potential dipole strength and its image, respectively.

Chapter 3

Hydrodynamics of Slender Rigid Rods Using Slender Body Theory

3.1   Singularity Methods for Slender Bodies

In this chapter, we consider a slender rigid rod with arc length s that is immersed in a viscous fluid and aim to compute the hydrodynamic loads exerted on each cross-section of the rod. In general, to determine the fluid velocity field around any arbitrary structure, one approach is to use the *boundary integral method* and fully solve the integral equations on the surface of the body[99, 59, 73, 83]. This method, however, provides more accuracy but computationally is intensive especially when there are multiple structures with complex geometries. Alternatively, the *singularity method* —also known as the *method of fundamental solutions*— is introduced to circumvent the computational difficulties associated with the boundary integral method. In this manner, the flow is represented by a line integral or point-wise distribution of appropriate singularities instead of a surface singularity distribution on the structure. Exclusively for a filament with a small but finite slenderness ratio, distribution of Stokeslets and potential dipoles along the center-line are necessary for the representation of the flow past the filament[83].

Here, we use slender body theory (SBT) which takes advantage of both the singularity method and the slenderness of the filament to reduce the boundary integral formulations into a single integral along the center-line of the filament. In SBT, the key idea is that the Stokeslets and potential dipoles with unknown strength can be distributed along the center-line of a slender filament. However, [40, 63, 45] showed that satisfying the no-slip boundary condition on the surface of a slender body of finite slenderness, requires the potential dipole's strength to be proportional to the perpendicular components of the Stokeslet's strength by a factor of $-a^2/4\mu$. The determination of each Stokeslet's strength $\mathbf{f}$ is crucial since it represents the hydro-

dynamic load per unit arc length exerted from the fluid on the corresponding cross-section of the filament. There is a various number of analytical methods presented in which an asymptotic expansion in terms of the slenderness ratio of the filament is used to examine the drag force distribution along the center-line of the filament[20, 4, 53, 56]. Later in this chapter, the theory of Cox, which employs the method of matched asymptotic expansion to analytically determine the hydrodynamic load exerted on the slender body from the nearby viscous fluid, will be discussed. In this section, we explore SBT and present a numerical algorithm for obtaining the stokeslets' strengths from which the fluid flow around the body will be identified.

Thanks to the linearity of the Stokes equations, the fluid velocity field around a slender filament can be determined at any arbitrary point ζ using the superposition of all singularity solutions distributed along the center-line of the filament. As discussed earlier in the previous chapter, the Green's function and the source singularities of the Stokes equations along with their higher-order derivatives, are all solutions to the Stokes flow. Higher-order singularity solutions for both source and force singularities including Dipoles, Quadrupoles, and Octupoles are well demonstrated by [95] and [83]. It is also shown that the Stokeslet Dipoles, Quadrupoles, etc. are found by taking the gradient ($\mathbf{\nabla}_0$) while source singularities —except the point source— by taking the laplacian ($\mathbf{\nabla}_0^2$) of the Stokes equation Green's function $\mathbf{G}(\mathbf{r}, \mathbf{r}_0) = \frac{\mathbf{I}}{r} + \frac{(\mathbf{r}-\mathbf{r}_0)(\mathbf{r}-\mathbf{r}_0)}{r^3}$ where subscript 0 is used to show that the operators are applied at $\mathbf{r}_0$ where the singularity exists. For instance, taking the laplacian of the Stokeslet and using the relation $\mathbf{D}(\mathbf{r}, \mathbf{r}_0) = -\frac{1}{2}\mathbf{\nabla}_0^2\mathbf{G}(\mathbf{r}, \mathbf{r}_0)$ which is given by (3.2), the potential dipole $\mathbf{D}(\mathbf{r}, \mathbf{r}_0)$ can be derived from the Stokeslet. In the context of this study, we confine our computations to the use of Stokeslets and potential dipoles only and neglect the inclusion of higher-order singularity solutions.

Now, by distributing the appropriate singularities along the center-line of the filament the velocity of the fluid at any arbitrary point ζ which will be marked by the vector $\mathbf{r}$, (see FIG. 2.1) is determined through:

$$\mathbf{u}(\mathbf{r}) = \mathbf{u}^\infty(\mathbf{r}) + \frac{1}{8\pi\mu}\int_0^L \mathbf{G}(\mathbf{r}, \mathbf{r}_0(s)) \cdot \mathbf{f}(s)\, ds + \frac{1}{4\pi}\int_0^L \mathbf{D}(\mathbf{r}, \mathbf{r}_0(s)) \cdot \mathbf{d}(s)\, ds \quad (3.1)$$

where the potential dipole is given by:

$$\mathbf{D}(\mathbf{r}, \mathbf{r}_0) = -\frac{\mathbf{I}}{r^3} + 3\frac{(\mathbf{r} - \mathbf{r}_0)(\mathbf{r} - \mathbf{r}_0)}{r^5} \quad (3.2)$$

and given by [63] the potential dipole strength $\boldsymbol{d}(s)$ is related to the normal component of the Stokeslets' strength $\boldsymbol{f}_\perp(s)$ through:

$$\mathbf{d}(s) = \left(\frac{-a^2}{4\mu}\right)\mathbf{f}_\perp(s) \quad (3.3)$$

Where, s is the arc length along the center-line, a is the radius, L is the length of the filament, and $\mathbf{D}$ is the potential dipole with strength $\mathbf{d}$. Note that, equation (6.4) is only valid for a filament immersed in an infinite unbounded fluid away from any rigid boundary.

In many applications, for instance the dense population of slender nanotubes attached to a solid plane forming nanocarpets [81, 77, 80] or slender bio-filaments cilia and flagella found attached or swimming close to a rigid wall [61], the presence of the rigid plane wall affects the hydrodynamic interactions between the filaments and the fluid. Thus, an extra no-slip boundary condition on the surface the rigid plane wall should be satisfied by the Stokes equations (2.3). Blake [8] used the method of images to satisfy the no-slip boundary condition on the surface of a rigid wall where the flow is induced by a point force placed at a distance h from the wall. He derived the appropriate singularity solutions $\mathbf{G}^w(\mathbf{r}, \mathbf{r}_0(s), \mathbf{r}_0^{im}(s))$ and $\mathbf{D}^w(\mathbf{r}, \mathbf{r}_0(s), \mathbf{r}_0^{im}(s))$ that are associated with the point force and the source doublet —also called the potential dipole— above the plane wall, respectively, in which the superscript im denotes the image of singularity solutions with respect to the wall (see FIG. 2.6). Replacing $\mathbf{G}(\mathbf{r}, \mathbf{r}_0(s), \mathbf{r}_0^{im}(s))$ with $\mathbf{G}^w(\mathbf{r}, \mathbf{r}_0(s), \mathbf{r}_0^{im}(s))$ and $\mathbf{D}(\mathbf{r}, \mathbf{r}_0(s))$ with $\mathbf{D}^w(\mathbf{r}, \mathbf{r}_0(s), \mathbf{r}_0^{im}(s))$ in equation (6.4) the fluid velocity field near the filament will be determined. The $\mathbf{G}^w$ and $\mathbf{D}^w$ are discussed in the previous chapter and are also given by [83, 43, 95]. Therefore, the fluid velocity field at any arbitrary point ζ, which will be marked by the vector $\mathbf{r}$, in the presence of an slender body swimming close to a plane wall yields:

$$
\begin{aligned}
\mathbf{u}(\mathbf{r}) = \mathbf{u}^\infty(\mathbf{r}) + &\frac{1}{8\pi\mu} \int_0^L \mathbf{G}^w(\mathbf{r}, \mathbf{r}_0(s), \mathbf{r}_0^{im}(s)) \cdot \mathbf{f}(s)\, ds + \\
&\frac{1}{4\pi} \int_0^L \mathbf{D}^w(\mathbf{r}, \mathbf{r}_0(s), \mathbf{r}_0^{im}(s)) \cdot \mathbf{d}(s)\, ds
\end{aligned}
\tag{3.4}
$$

The solution of (3.4) requires the point force density $\mathbf{f}(s)$ to be determined at each cross-section of the rod. To evaluate the strength and the direction of the force at each cross-section, the no-slip boundary condition on the surface of the rod, which states the velocity of each cross-section should match the summation of induced fluid velocities by the rest of the Stokeslets at that specific material point, should be satisfied. Given the velocity of each infinitesimal cross-section of the rod $\boldsymbol{v}$, equation (3.5) provides us with a system of linear equations that needs to be inverted to obtain the hydrodynamic load $\mathbf{f}$ at each cross-section of the rod. Now, to present an integrable numerical method, we follow the method by [84, 43] and use equation (3.5)

in which $1 \leq i, j \leq N$:

$$
\begin{aligned}
\boldsymbol{v}(s_i) =& \mathbf{u}^\infty(s_i) + \left(\frac{1}{c_\perp} \boldsymbol{f}_\perp(s_i) \right) + \left(\frac{1}{c_\parallel} \boldsymbol{f}_\parallel(s_i) \right) + \\
& \frac{1}{8\pi\mu} \sum_{j=1, j\neq i}^{N} \mathbf{G}^w(\mathbf{r}(s_i), \mathbf{r}_0(s_j), \mathbf{r}_0^{im}(s_j)) \cdot \mathbf{f}(s_j) \, \Delta s + \\
& \frac{1}{4\pi} \sum_{j=1, j\neq i}^{N} \mathbf{D}^w(\mathbf{r}(s_i), \mathbf{r}_0(s_j), \mathbf{r}_0^{im}(s_j)) \cdot \mathbf{d}(s_j) \, \Delta s
\end{aligned}
\tag{3.5}
$$

where $\boldsymbol{f}_\perp$ and $\boldsymbol{f}_\parallel$ denote the normal and tangential components of the force, $c_\parallel$ and $c_\perp$ are the resistive drag coefficients for each small section of the rod given by $2\pi\mu/(\ln{(2q/a)} - 0.5)$ and $4\pi\mu/(\ln{(2q/a)} + 0.5)$ respectively, in which $q = \frac{a}{2}\sqrt{e} \simeq 0.82a$ is a natural cut-off length. For $\mathbf{f} \in \mathbb{R}^3$, (3.5) provides us with 3N linear equations that can be inverted to obtain the 3N unknown force strengths. In this manner, we find the 3N vector $\mathbf{B}$, which includes all the unknown force strengths, through $\mathbf{B} = \mathbf{A}^{-1}\mathbf{C}$ in which $\mathbf{A}$ is the 3N×3N coefficient matrix, and $\mathbf{C}$ identifies a 3N vector that includes the known values of the relative velocity at each cross-sections along the filament.

To construct the components of the coefficient matrix $\mathbf{A}$ let $1 \leq n, k \leq 3$ then following [51, 81] we introduce (3.6):

$$
A_{3(i-1)+n, 3(j-1)+k} =
$$

$$
\begin{cases}
\frac{1}{c_\parallel}(\hat{\mathbf{t}}\hat{\mathbf{t}})^T + \frac{1}{c_\perp}(\hat{\mathbf{I}} - \hat{\mathbf{t}}\hat{\mathbf{t}})^T + \\
\frac{\Delta s}{8\pi\mu} \left[G_{nk}^{im}(\mathbf{r}(s_i), \mathbf{r}_0^{im}(s_j)) + \frac{-a^2}{2} D_{nk}^{im}(\mathbf{r}(s_i), \mathbf{r}_0^{im}(s_j))(\hat{\mathbf{I}} - \hat{\mathbf{t}}\hat{\mathbf{t}}) \right] & \text{if } i = j \\
\\
\frac{\Delta s}{8\pi\mu} \left[G_{nk}^{w}(\mathbf{r}(s_i), \mathbf{r}_0(s_j), \mathbf{r}_0^{im}(s_j)) + \frac{-a^2}{2} D_{nk}^{w}(\mathbf{r}(s_i), \mathbf{r}_0(s_j), \mathbf{r}_0^{im}(s_j))(\hat{\mathbf{I}} - \hat{\mathbf{t}}\hat{\mathbf{t}}) \right] & \\
& \text{if } i \neq j
\end{cases}
\tag{3.6}
$$

Let define $\mathbf{G}^{im}$ and $\mathbf{D}^{im}$ such that $\mathbf{G}^{im} = \mathbf{G}^w - \mathbf{G}$ and $\mathbf{D}^{im} = \mathbf{D}^w - \mathbf{D}$ when $\mathbf{G}$ and $\mathbf{G}^w$ are given by equations (2.4) and (2.23), and $\mathbf{D}$ and $\mathbf{D}^w$ given by (2.32) and (2.38), respectively. Here $\hat{\mathbf{I}} = \hat{\mathbf{t}}\hat{\mathbf{t}} + \hat{\mathbf{n}}\hat{\mathbf{n}} + \hat{\mathbf{b}}\hat{\mathbf{b}}$ while $\hat{\mathbf{t}}$, $\hat{\mathbf{n}}$, and $\hat{\mathbf{b}}$ denote the unit tangent, normal, and binormal vectors evaluated at $s = s_i$, respectively. The 3N vector $\mathbf{C}$ consisting the known relative velocities between the filament and the far-field flow at each cross section is given by:

$$
C_{3(i-1)+n} = v_n(s_i) - u_n^\infty(s_i)
\tag{3.7}
$$

therefore the $3N$ vector $\mathbf{B} = [\mathbf{f}_1 \ \mathbf{f}_2 \ ... \ \mathbf{f}_N]^T$ which includes the unknowns Stokeslets strengths will be found.

Now, the results from slender body theory (SBT) which are obtained computationally, are compared with the resistive force theory (RFT). In the following cases, the rod is taken to be straight while moving perpendicular to the flow with a predefined velocity profile. In FIG. 3.1, an straight rigid filament is subjected to a shear flow in which the velocity profile is linearly changing from zero at the base up to the tip of the filament and the corresponding force densities are obtained using RFT and SBT.
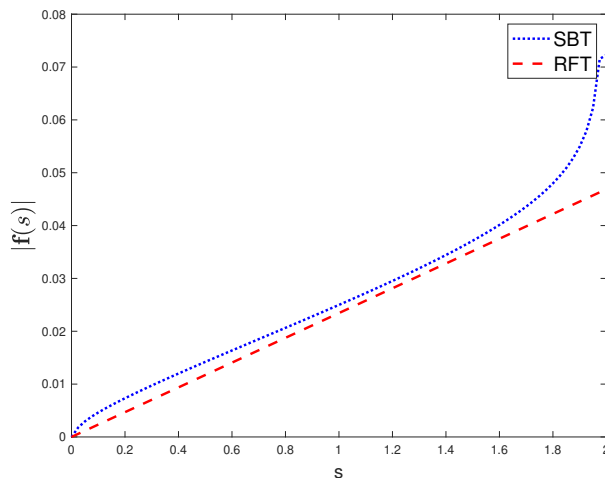
Figure 3.1: Computation of the hydrodynamic loads on each cross-section of a straight rod attached to a plane wall using slender body theory (SBT) and resistive force theory (RFT)

3.2 Slender Body Theory of Cox

The general slender body theory (SBT) presented by Cox [20] considers all the disturbances produced by a slender body which is immersed in an unbounded viscous fluid at low Reynolds numbers. An analytical solution for the drag force per unit arc length along the body of the slender filament is found using asymptotic methods in terms of the slenderness ratio of the rod. The expression for the drag force provided by Cox is valid when the filament has a small slenderness ratio $\varepsilon = a/L$ in which a is the maximum radius and L is the length of the filament so that the corresponding error approximation will be found in the order of $1/(\ln \varepsilon)^3$. Implementation of the

Cox SBT requires the geometry of the rod to be known so that the drag force per unit arc length of the rod $\mathbf{f}(s)$ at each cross-section of the rod can be computed, in which s denotes the arc length of the rigid filament. Here, we first consider a vertical rigid rod with a constant circular cross-section in an unbounded fluid, which undergoes a uniform translation perpendicular to the center-line of the rod. We then compute the hydrodynamic drag force that is exerted on each cross-section of the rigid rod.

The formulation in equation (3.8) explicitly defines the local drag force per unit arc length $\mathbf{f}(s)$, in terms of the relative velocity of the fluid $\mathbf{u}^\infty(s) - \boldsymbol{v}(s)$ at each cross-section of the rigid rod. Here, $\mathbf{u}^\infty(s)$ denotes the fluid velocity at far-field, and $\boldsymbol{v}(s)$ represents the velocity of the cross-section located at s, which due to the no-slip boundary condition is equivalent to the velocity of the fluid on the body of the filament at the similar point. The force distribution along the rigid filament with constant radius of a at any cross-section, yields:

$$\frac{\mathbf{f}(s)}{2\pi\mu} = \left(\frac{\mathbf{u}^\infty(s) - \boldsymbol{\nu}(s)}{\ln\varepsilon} + \frac{\mathbf{J}(s) + (\mathbf{u}^\infty(s) - \boldsymbol{\nu}(s))\ln(2\epsilon)}{(\ln\varepsilon)^2} \right) \cdot (\mathbf{tt} - 2\mathbf{I})$$
$$+ \frac{\mathbf{u}^\infty(s) - \boldsymbol{\nu}(s)}{2(\ln\varepsilon)^2} \cdot (3\mathbf{tt} - 2\mathbf{I}) + O\left(\frac{1}{(\ln\varepsilon)^3}\right) \tag{3.8}$$

Where $\mathbf{I}$ is the identity tensor, and $\mathbf{t} = \mathbf{t}(s)$ represents the unit tangent vector along the filament at s. The vector $\mathbf{J}$ is also given by :

$$\mathbf{J}(s) = -\frac{1}{2}\left[\int_0^{s-\epsilon} + \int_{s+\epsilon}^L\right]\left(\frac{\mathbf{I}}{\hat{r}} + \frac{\hat{\boldsymbol{x}}\hat{\boldsymbol{x}}}{\hat{r}^3}\right) \times \left(\mathbf{I} - \frac{1}{2}\hat{\mathbf{t}}\hat{\mathbf{t}}\right) \cdot (\mathbf{u}^\infty(\hat{s}) - \boldsymbol{\nu}(\hat{s}))d\hat{s} \tag{3.9}$$

in which $\hat{\mathbf{t}} = \mathbf{t}(\hat{s})$, the vector $\hat{x} = \mathbf{r}_0(\hat{s}) - \mathbf{r}_0(s)$ with $\hat{r} = |\hat{\boldsymbol{x}}|$, and ϵ be an arbitrary parameter chosen between $0 < \epsilon \ll 1$. It should be noted that the formulations above given for non-local hydrodynamic interactions are only valid approximations when the body does not experience any self-interactions, otherwise, the singular solutions may arise[96]. The integration in equation (3.9) should also be taken with care since a singularity exists at $s = \hat{s}$. To avoid the numerical issues, the ϵ should be chosen such that $\epsilon = \Delta s$ where Δs denotes the length of each element after discretization of the rod. Therefore, the smaller the value of the ϵ, the smaller the value of Δs is required to be employed, which may be accompanied by higher computational costs especially for the simulation of multiple arrays of filaments.

Analytically integrating the equation (3.8,3.9) for a straight rigid rod such that $\mathbf{t}$ holds a constant value, the total drag force can readily be determined. The total hydrodynamic load acting on the rod can be written as

$$\mathbf{F} = \xi_t(\mathbf{U} \cdot \mathbf{t})\mathbf{t} + \xi_n(\mathbf{U} \cdot \mathbf{n})\mathbf{n} + \xi_b(\mathbf{U} \cdot \mathbf{b})\mathbf{b} \tag{3.10}$$

where $\mathbf{t}$, $\mathbf{n}$, and $\mathbf{b}$ respectively denote the unit tangent vector, unit normal vector, and the unit bi-normal vector along the straight rod. Then let $\mathbf{U} = \mathbf{u}^\infty - \boldsymbol{\nu}$ while
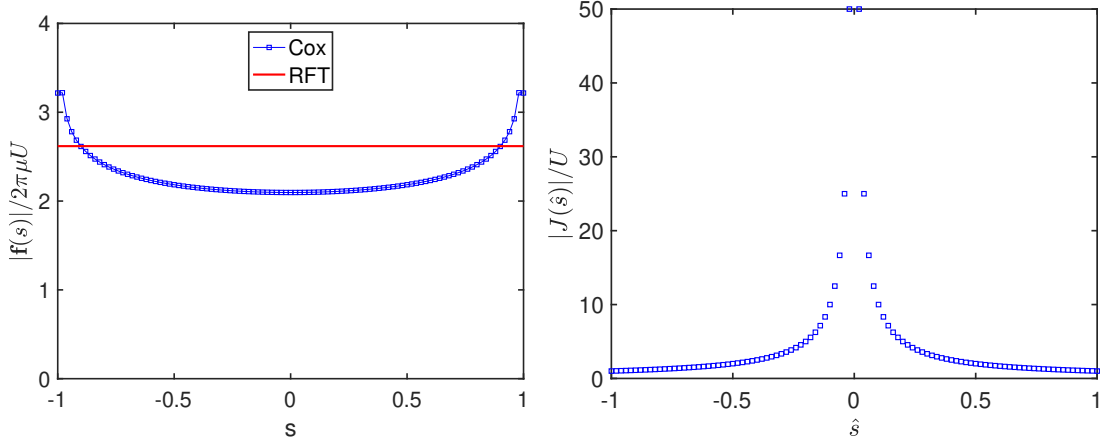
Figure 3.2: In the following figures, a rigid circular cylinder is assumed to be sedimenting perpendicular to the unit tangent vector of the slender body with velocity $U = |\boldsymbol{U}|$ in an unbounded fluid at rest. On the left side, the non-dimensional drag force per unit arc length of the rigid rod using RFT and SBT, are compared. On the right side, the integrand of $\boldsymbol{J}(s)$, which is denoted by $\boldsymbol{J}(\hat{s})$, at a typical point $s = 0.5$ is shown. The simulation parameters for this figure are as follows: the slenderness $\varepsilon = 0.01$, $\epsilon = \Delta s = 0.01$ while the position of each cross-section is marked with s where $-1 < s < 1$.

both $\mathbf{u}^\infty$ and $\boldsymbol{\nu}$ are assumed to be constant along s. Here, ξ_t, ξ_n, and ξ_b represent the drag coefficients along the unit vectors $\mathbf{t}$, $\mathbf{n}$, and $\mathbf{b}$, respectively, and are given as:

$$\xi_t = -\frac{2\pi\mu L}{\ln\left(\varepsilon^{-1}\right) + Z_1} \tag{3.11}$$

$$\xi_n = \xi_b = -\frac{4\pi\mu L}{\ln\left(\varepsilon^{-1}\right) + Z_2} \tag{3.12}$$

It is shown that for a circular cylinder $Z_1 \simeq -0.81$ and $Z_2 = Z_1 + 1$. We should note that for a slender body the drag coefficients along $\mathbf{n}$ and $\mathbf{b}$ do not vary significantly thus we can write $\xi_n = \xi_b$. Local drag coefficients are also obtained through the leading order term in equation (3.8). For an infinitely long slender filament, the higher-order terms of the expansion can be neglected since the first term which is of order $1/(\ln \varepsilon)$ becomes the dominant term[96]. Thus, the drag force per unit length for an slender filament with small slenderness ratio $\varepsilon = a/L \ll 1$, will reduce to $\xi_t^* = -2\pi\mu/\ln\left(\varepsilon^{-1}\right)$ while $\xi_n^* = \xi_b^* = 2\xi_t^*$. In this case, the SBT is reduced to the *resistive force theory* or (RFT) where a linear relationship between the drag force and the fluid velocity per unit arc length of the filament is maintained. Generally, RFT is considered as a simpler version of the slender body theory (SBT) with the

31

contribution of the leading order terms only, which provides less complexity and accuracy to the problem. It should also be noted that Gray and Hancock [40] was the first who introduced the local hydrodynamic drag coefficients using the linear superposition of singularities along the center-line of the filament.

Chapter 4

Dynamics of Slender elastic filaments

4.1   Computational Rod Model

Now in this chapter, we turn our attention towards the dynamics of slender structures. A continuum rod model that captures the dynamics of the elastic rod, in general, employs the dynamic equilibrium equations and the compatibility equations that should be solved together whether symbolically or numerically. However, the symbolic approach should be avoided due to the intensive computational costs, and instead, a robust numerical method must be developed to computationally solve the sets of nonlinear differential equations[27]. Besides, the constitutive equation, which defines the relation between the internal moments and the curvature along the elastic rod, completes the required equations for integration with respect to space and time once the appropriate boundary and initial conditions are readily at hand. It should be noted that the identification of the constitutive parameters might be challenging, especially for biological filaments that are consist of complex internal structures. In such sophisticated systems, inverse approaches as introduced by [27, 28] can be implemented to determine the exact functional form of the constitutive parameters which may vary along the filament.

Here, the continuum rod model that we use for tracking the elastic deformations of a slender filament follows the classical approach of the Kirchhoff [58] which assumes each cross-section of the rod to be rigid. Thus, the rod needs to be the discretized in space and time so that the equations of equilibrium and compatibility along with the constitutive equation can be solved simultaneously at each cross-section of the rod to determine the unknown information. Following [38, 28, 27, 92, 34], equations of equilibrium (4.1) and (4.2) along with the equations of compatibility (4.3) and (4.4)

are given below:

$$m(\frac{\partial \boldsymbol{v}}{\partial t} + \boldsymbol{\omega} \times \boldsymbol{v}) - (\frac{\partial \boldsymbol{f}}{\partial s} + \boldsymbol{\kappa} \times \boldsymbol{f}) - \boldsymbol{f}^{ext} = \boldsymbol{0} \tag{4.1}$$

$$\boldsymbol{I}_m \frac{\partial \boldsymbol{\omega}}{\partial t} + \boldsymbol{\omega} \times \boldsymbol{I}_m \boldsymbol{\omega} - (\frac{\partial \boldsymbol{q}}{\partial s} + \boldsymbol{\kappa} \times \boldsymbol{q}) - \mathbf{r}_s \times \boldsymbol{f} - \boldsymbol{q}^{ext} = \boldsymbol{0} \tag{4.2}$$

$$\frac{\partial \mathbf{r}_s}{\partial t} + \boldsymbol{\omega} \times \mathbf{r}_s - (\frac{\partial \boldsymbol{v}}{\partial s} + \boldsymbol{\kappa} \times \boldsymbol{v}) = \boldsymbol{0} \tag{4.3}$$

$$\frac{\partial \boldsymbol{\kappa}}{\partial t} - (\frac{\partial \boldsymbol{\omega}}{\partial s} + \boldsymbol{\kappa} \times \boldsymbol{\omega}) = \boldsymbol{0} \tag{4.4}$$

The first two equations respectively represent the balance of linear and angular momentum, in which t is time, s is the arc length along the center-line, m is the mass per unit length of the rod, $\boldsymbol{I}_m$ is the 3 by 3 tensor of moment of inertia per unit length, and the spatial derivative of vector $\mathbf{r}_0(s,t)$, which marks the position of each cross-section here, is denoted by the vector $\mathbf{r}_s$. The vectors $\boldsymbol{v}(s,t)$ and $\boldsymbol{\omega}(s,t)$ capture the linear and angular velocity of the cross-sections respectively, $\boldsymbol{\kappa}(s,t)$ defines the curvature and the twist vectors, and the net internal force and internal moment over each cross-section of the rod are denoted by vectors $\boldsymbol{f}(s,t)$ and $\boldsymbol{q}(s,t)$, respectively [27, 28]. The constitutive law with an algebraic form of $\boldsymbol{q}(s,t) = \mathbf{B}(s)(\boldsymbol{\kappa}(s,t) - \boldsymbol{\kappa}_0(s))$ is used where the matrix $\mathbf{B}$ encodes the bending and torsional stiffness moduli of the rod, and $\boldsymbol{\kappa}_0(s)$ describes the initial stress-free curvature and twist vector. Thus, the internal restoring moment $\boldsymbol{q}(s,t)$ can readily be substituted in the equation (4.2). In the context of this study, we limit ourselves to the use of zero initial curvature and twist configuration $\boldsymbol{\kappa}_0(s) = \boldsymbol{0}$, along with the choice of constant constitutive properties, which are given as:

$$\mathbf{B} = \begin{bmatrix} EI_1 & 0 & 0 \\ 0 & EI_2 & 0 \\ 0 & 0 & GI_3 \end{bmatrix} \tag{4.5}$$

in which I_1, I_2 denote the second moment of area along the bending axes within the body-fixed frame which are represented by the normal $\boldsymbol{n}$ and bi-normal $\boldsymbol{b}$ unit vectors, and I_3 along the twist axis, which is represented by the unit vector $\boldsymbol{t}$. Any external forces and moments imposed on cross-sections are captured by vectors $\boldsymbol{f}^{ext}(s,t)$ and $\boldsymbol{q}^{ext}(s,t)$ respectively. In our fluid-structure interaction model, the fluid and the structure communicate with each other through the vectors $\boldsymbol{f}^{ext}$ and $\boldsymbol{q}^{ext}$ in which the external hydrodynamic loads can be computed by the slender-body theory. Moreover, we should note that at low Reynolds numbers regime where the inertial effects are

very negligible the general form of equations (4.1-4.4) can specifically be reduced to the following sets of equations:

$$(\frac{\partial \boldsymbol{f}}{\partial s} + \boldsymbol{\kappa} \times \boldsymbol{f}) + \boldsymbol{f}^{ext} = \boldsymbol{0} \tag{4.6}$$

$$(\mathbf{B}\frac{\partial \boldsymbol{\kappa}}{\partial s} + \boldsymbol{\kappa} \times \mathbf{B}\boldsymbol{\kappa}) + \boldsymbol{t} \times \boldsymbol{f} + \boldsymbol{q}^{ext} = \boldsymbol{0} \tag{4.7}$$

$$(\frac{\partial \boldsymbol{v}}{\partial s} + \boldsymbol{\kappa} \times \boldsymbol{v}) - \boldsymbol{\omega} \times \boldsymbol{t} = \boldsymbol{0} \tag{4.8}$$

$$(\frac{\partial \boldsymbol{\omega}}{\partial s} + \boldsymbol{\kappa} \times \boldsymbol{\omega}) - \frac{\partial \boldsymbol{\kappa}}{\partial t} = \boldsymbol{0} \tag{4.9}$$

In equation (4.8), the inextensibility constraint conserves the arc length locally by imposing $r_s = \boldsymbol{t}$ where $\boldsymbol{t} = (0, 0, 1)$ represents the unit tangent vector along the center-line of the slender rod when measured with respect to the body fixed frame. Thus, the unshearability constraint $\frac{\partial \mathbf{r}_s}{\partial t} = \boldsymbol{0}$ will be satisfied as well. Also note that in equation (4.7), the net internal moment $\boldsymbol{q}$ is directly replaced with $\mathbf{B}\boldsymbol{\kappa}$ where $\mathbf{B}$ holds the constant values of constitutive parameters corresponding to the bending and torsional stiffness, identified by the equation (4.5). Now, four partial differential equations in 3-dimensional space are left, and the four unknown vectors $\boldsymbol{v}(s, t)$, $\boldsymbol{\omega}(s, t)$, $\boldsymbol{\kappa}(s, t)$, and $\boldsymbol{f}(s, t)$ need to be determined. The aforementioned assembled system of equations presented by [34, 38, 28] is used and combined with a numerical integration scheme by which the unknown vectors will be obtained at each time step and at every node along the flexible slender rod.

4.2   System of Assembled Equations

Rearranging equations (4.6-4.9) that represent the equations of motion for an inextensible/unshearable rod with negligible inertia, they are written in a more compact form as:

$$\mathbf{M}\frac{\partial \mathbf{Y}}{\partial t} + \mathbf{K}\frac{\partial \mathbf{Y}}{\partial s} + \mathbf{F} = \boldsymbol{0} \tag{4.10}$$

In which, $\mathbf{Y}$ holds a 12×1 column vector of unknowns given by:

$$\mathbf{Y} = \begin{bmatrix} \boldsymbol{v} \\ \boldsymbol{\omega} \\ \boldsymbol{\kappa} \\ \boldsymbol{f} \end{bmatrix} \tag{4.11}$$

Note that we have rearranged the sets of partial differential equations in the following order: equation (4.8) first, (4.9) second, (4.7) third, and (4.6) which is

settled as the last equation. This is done to fill the diagonal inputs of the matrix $\mathbf{K}$ with the corresponding coefficients rather than the off-diagonal terms. The $\mathbf{M}$ and $\mathbf{K}$ that we respectively call the mass and stiffness matrix, are 12×12 matrices that contain the coefficients of the partial differentials of the unknown vectors:

$$
\mathbf{M} = \begin{bmatrix} \mathbf{O} & \mathbf{O} & \mathbf{O} & \mathbf{O} \\ \mathbf{O} & \mathbf{O} & -\mathbf{I} & \mathbf{O} \\ \mathbf{O} & \mathbf{O} & \mathbf{O} & \mathbf{O} \\ \mathbf{O} & \mathbf{O} & \mathbf{O} & \mathbf{O} \end{bmatrix} \quad , \quad \mathbf{K} = \begin{bmatrix} \mathbf{I} & \mathbf{O} & \mathbf{O} & \mathbf{O} \\ \mathbf{O} & \mathbf{I} & \mathbf{O} & \mathbf{O} \\ \mathbf{O} & \mathbf{O} & \mathbf{B} & \mathbf{O} \\ \mathbf{O} & \mathbf{O} & \mathbf{O} & \mathbf{I} \end{bmatrix} \tag{4.12}
$$

where $\mathbf{I}$ represents the 3×3 identity matrix and $\mathbf{O}$ shows a null 3×3 matrix. The 12×1 column vector $\mathbf{F}$ contains all of the non-homogeneous terms, and is expressed through:

$$
\mathbf{F} = \begin{bmatrix} \boldsymbol{\kappa} \times \boldsymbol{v} - \boldsymbol{\omega} \times \boldsymbol{t} \\ \boldsymbol{\kappa} \times \boldsymbol{\omega} \\ \boldsymbol{\kappa} \times \mathbf{B}\boldsymbol{\kappa} + \boldsymbol{t} \times \boldsymbol{f} + \boldsymbol{q}^{ext} \\ \boldsymbol{\kappa} \times \boldsymbol{f} + \boldsymbol{f}^{ext} \end{bmatrix} \tag{4.13}
$$

Now, the partial differential equations need to be integrated in space and time but the nonlinearity of the non-homogeneous vector $\mathbf{F}$ requires us to employ an iterative procedure which will be discussed next.

4.3   Numerical Algorithm

Generalized-α method is a robust integration algorithm [15] that we adopt to solve the sets of slender rod equations given in a compact form by equation (4.10). However, obtaining the solution for the 12 unknowns in equation (4.10) requires 12 boundary conditions to be determined and implemented in the problem at each time step (recall that each unknown vector contains 3 unknowns in 3-dimensional space so that 4 unknown vectors $\boldsymbol{v}$, $\boldsymbol{\omega}$, $\boldsymbol{\kappa}$, and $\boldsymbol{f}$ overall have 12 unknowns and therefore 12 boundary conditions are required). We also use the method of incremental rotation [10, 39, 29] to transform the body-fixed frame to the inertial reference frame.

Using the *Generalized-α* algorithm, discretization of the equation (4.10) yields:

$$
\mathbf{M}_{1-\beta_s}^{1-\beta_t} \left(\frac{\partial \mathbf{Y}}{\partial t} \right)_{1-\alpha_s}^{1-\alpha_t} + \mathbf{K}_{1-\beta_s}^{1-\beta_t} \left(\frac{\partial \mathbf{Y}}{\partial s} \right)_{1-\beta_s}^{1-\beta_t} + \mathbf{F}_{1-\beta_s}^{1-\beta_t} = \mathbf{0} \tag{4.14}
$$

Let the following notation for any quantity $\mathbf{W}$ [38, 27] represent:

$$
\begin{aligned}
\mathbf{W}^{1-\alpha} &= (1-\alpha)\mathbf{W}^i + \alpha\mathbf{W}^{i-1} \\
\mathbf{W}_{1-\alpha} &= (1-\alpha)\mathbf{W}_j + \alpha\mathbf{W}_{j-1}
\end{aligned} \tag{4.15}
$$

such that i defines a grid point discretized in time and j in space. In this study, we use linear and homogeneous constitutive parameters and rod properties, thus the mass $\mathbf{M}$ and the stiffness $\mathbf{K}$ matrices are constant and do not vary with the time t and space s. The equation above can be written in the simplified form of:

$$\mathbf{M}\left(\frac{\partial \mathbf{Y}}{\partial t}\right)^{1-\alpha_t}_{1-\alpha_s} + \mathbf{K}\left(\frac{\partial \mathbf{Y}}{\partial s}\right)^{1-\beta_t}_{1-\beta_s} + \mathbf{F}^{1-\beta_t}_{1-\beta_s} = \mathbf{0} \tag{4.16}$$

To solve equation (4.16), first we need to discretize it in space and construct the assembled matrices in terms of $\mathbf{Y}$ and $\frac{\partial \mathbf{Y}}{\partial t}$. Here, we choose the parameters $\alpha_s = \beta_s = 0.5$ to evaluate each differential equation at the middle of grid-points j and $j-1$. In this manner, equation (4.17) needs to be discretized in space first:

$$\mathbf{M}\left(\dot{\mathbf{Y}}\right)_{\frac{1}{2}} + \mathbf{K}\left(\mathbf{Y}'\right)_{\frac{1}{2}} + \left(\mathbf{F}\right)_{\frac{1}{2}} = \mathbf{0} \tag{4.17}$$

where the notations $\dot{\mathbf{Y}} = \frac{\partial \mathbf{Y}}{\partial t}$ for the time derivatives and $\mathbf{Y}' = \frac{\partial \mathbf{Y}}{\partial s}$ for the spatial derivatives are used. Extensively for the spatial derivative at each mid grid-point we define:

$$\left(\mathbf{Y}'\right)_{\frac{1}{2}} = \frac{\mathbf{Y}_\mathbf{j} - \mathbf{Y}_{\mathbf{j}-1}}{\Delta s} \tag{4.18}$$

but for $\left(\dot{\mathbf{Y}}\right)_{\frac{1}{2}}$ and $\left(\mathbf{F}\right)_{\frac{1}{2}}$ we follow the generalized-α discretization instruction provided by (4.15). As a result, we arrive at the following equation:

$$\frac{1}{2}\mathbf{M}\left(\dot{\mathbf{Y}}_j + \dot{\mathbf{Y}}_{j-1}\right) + \frac{1}{\Delta s}\mathbf{K}\left(\mathbf{Y}_\mathbf{j} - \mathbf{Y}_{\mathbf{j}-1}\right) + \frac{1}{2}\left(\mathbf{F}_j + \mathbf{F}_{j-1}\right) = \mathbf{0} \tag{4.19}$$

Let the filament be discretized into $N-1$ segments such that the index j takes the values $1 \le j \le N$. Now, the whole $12 \times (N-1)$ PDEs along with the 12 boundary equations can be written in using the following assembled matrices:

$$\widetilde{\mathbf{M}} = \begin{bmatrix} \mathbf{M} & \mathbf{M} & \boldsymbol{O} & \cdots & \boldsymbol{O} \\ \boldsymbol{O} & \mathbf{M} & \mathbf{M} & \boldsymbol{O} & \vdots \\ \vdots & \ddots & \ddots & \ddots & \boldsymbol{O} \\ \boldsymbol{O} & \cdots & \boldsymbol{O} & \mathbf{M} & \mathbf{M} \\ \boldsymbol{O} & \cdots & \cdots & \cdots & \boldsymbol{O} \end{bmatrix}_{12N \times 12N},$$

$$\widetilde{\mathbf{K}} = \frac{2}{\Delta s}\begin{bmatrix} -\mathbf{K} & \mathbf{K} & \boldsymbol{O} & \cdots & \boldsymbol{O} \\ \boldsymbol{O} & -\mathbf{K} & \mathbf{K} & \boldsymbol{O} & \vdots \\ \vdots & \ddots & \ddots & \ddots & \boldsymbol{O} \\ \boldsymbol{O} & \cdots & \boldsymbol{O} & -\mathbf{K} & \mathbf{K} \\ \boldsymbol{I}_L\left(\frac{\Delta s}{2}\right) & \cdots & \cdots & \cdots & \boldsymbol{I}_R\left(\frac{\Delta s}{2}\right) \end{bmatrix}_{12N \times 12N} \tag{4.20}$$

37

where $\boldsymbol{O}$ denotes a 12×12 null matrix. The vectors $\widetilde{\dot{\mathbf{Y}}}$, $\widetilde{\mathbf{Y}}$, and $\widetilde{\mathbf{F}}$ are given by:

$$\widetilde{\dot{\mathbf{Y}}} = \begin{bmatrix} \dot{\mathbf{Y}}_1 \\ \dot{\mathbf{Y}}_2 \\ \vdots \\ \dot{\mathbf{Y}}_N \end{bmatrix}_{12N} \quad , \quad \widetilde{\mathbf{Y}} = \begin{bmatrix} \mathbf{Y}_1 \\ \mathbf{Y}_2 \\ \vdots \\ \mathbf{Y}_N \end{bmatrix}_{12N} \quad , \quad \widetilde{\mathbf{F}} = \begin{bmatrix} \mathbf{F}_1 + \mathbf{F}_2 \\ \mathbf{F}_2 + \mathbf{F}_3 \\ \vdots \\ \mathbf{F}_{N-1} + \mathbf{F}_N \\ \mathbf{BC} \end{bmatrix}_{12N} \tag{4.21}$$

The last row represents the 12 required equations for the boundary conditions. In the context of this study, we consider a filament which is clamped at $s = 0$ and free at the other end $s = L$. Therefore, the boundary conditions appropriate to such problem requires $\boldsymbol{v} = \boldsymbol{\omega} = \mathbf{0}$ at $s = 0$, and $\boldsymbol{\kappa} = \boldsymbol{f} = \mathbf{0}$ at $s = L$. Thus, the 12×12 matrices $\boldsymbol{I}_L$ and $\boldsymbol{I}_R$, along with the 12×1 vector $\mathbf{BC}$, become:

$$\boldsymbol{I}_L = \begin{bmatrix} \mathbf{I} & \mathbf{O} & \mathbf{O} & \mathbf{O} \\ \mathbf{O} & \mathbf{I} & \mathbf{O} & \mathbf{O} \\ \mathbf{O} & \mathbf{O} & \mathbf{O} & \mathbf{O} \\ \mathbf{O} & \mathbf{O} & \mathbf{O} & \mathbf{O} \end{bmatrix} \quad , \quad \boldsymbol{I}_R = \begin{bmatrix} \mathbf{O} & \mathbf{O} & \mathbf{O} & \mathbf{O} \\ \mathbf{O} & \mathbf{O} & \mathbf{O} & \mathbf{O} \\ \mathbf{O} & \mathbf{O} & \mathbf{I} & \mathbf{O} \\ \mathbf{O} & \mathbf{O} & \mathbf{O} & \mathbf{I} \end{bmatrix} \quad , \quad \mathbf{BC} = \begin{bmatrix} \mathbf{O} \\ \mathbf{O} \\ \mathbf{O} \\ \mathbf{O} \end{bmatrix} \tag{4.22}$$

in which $\mathbf{I}$ is 3×3 identity matrix. As a result, the compact form equations can be written as:

$$\widetilde{\mathbf{M}}\widetilde{\dot{\mathbf{Y}}} + \widetilde{\mathbf{K}}\widetilde{\mathbf{Y}} + \widetilde{\mathbf{F}} = \mathbf{0} \tag{4.23}$$

However, equation (4.23) is continuous in time [64] and needs to be integrated. Following the generalized-α method we obtain:

$$\left(\widetilde{\mathbf{M}}\widetilde{\dot{\mathbf{Y}}} \right)^{1-\alpha_t} + \left(\widetilde{\mathbf{K}}\widetilde{\mathbf{Y}} \right)^{1-\beta_t} + \left(\widetilde{\mathbf{F}} \right)^{1-\beta_t} = \mathbf{0} \tag{4.24}$$

The matrices $\widetilde{\mathbf{M}}$ and $\widetilde{\mathbf{K}}$ are constant and do not change with time, thus (4.24) reduces to:

$$\widetilde{\mathbf{M}}\left((1-\alpha_t)\widetilde{\dot{\mathbf{Y}}}^i + (\alpha_t)\widetilde{\dot{\mathbf{Y}}}^{i-1} \right) + \widetilde{\mathbf{K}}\left((1-\beta_t)\widetilde{\mathbf{Y}}^i + (\beta_t)\widetilde{\mathbf{Y}}^{i-1} \right) + \left((1-\beta_t)\widetilde{\mathbf{F}}^i + (\beta_t)\widetilde{\mathbf{F}}^{i-1} \right) = \mathbf{0} \tag{4.25}$$

Again using the Newmark algorithm, the time derivative can be approximated by:

$$\left(\dot{\mathbf{Y}} \right)^i = \frac{\mathbf{Y}^i - \mathbf{Y}^{i-1}}{\gamma_t \Delta t} - \frac{1 - \gamma_t}{\gamma_t} \left(\dot{\mathbf{Y}} \right)^{i-1} \tag{4.26}$$

substituting (4.26) into (4.25) yields:

$$
\overbrace{\left(\widetilde{\mathbf{M}}(1-\alpha_t)(\frac{1}{\gamma_t\Delta t}) + \widetilde{\mathbf{K}}(1-\beta_t)\right)}^{\Xi_1}\widetilde{\mathbf{Y}}^i + \overbrace{\left(\widetilde{\mathbf{M}}(1-\alpha_t)(\frac{-1}{\gamma_t\Delta t}) + \widetilde{\mathbf{K}}(\beta_t)\right)}^{\Xi_2}\widetilde{\mathbf{Y}}^{i-1}+
$$
$$
\underbrace{\widetilde{\mathbf{M}}\left((1-\alpha_t)(\frac{\gamma_t-1}{\gamma_t}) + (\alpha_t)\right)}_{\Xi_3}\dot{\widetilde{\mathbf{Y}}}^{i-1} + \left((1-\beta_t)\widetilde{\mathbf{F}}^i + (\beta_t)\widetilde{\mathbf{F}}^{i-1}\right) = \mathbf{0}
\tag{4.27}
$$

which can be written in a compact form as

$$
\Xi_1\widetilde{\mathbf{Y}}^i + \Xi_2\widetilde{\mathbf{Y}}^{i-1} + \Xi_3\dot{\widetilde{\mathbf{Y}}}^{i-1} + (1-\beta_t)\widetilde{\mathbf{F}}^i + (\beta_t)\widetilde{\mathbf{F}}^{i-1} = \mathbf{0}
\tag{4.28}
$$

Therefore, to determine the unknown vector $\widetilde{\mathbf{Y}}^i$, equation (4.28) needs to be solved. However, the presence of the nonlinear and unknown term $\widetilde{\mathbf{F}}^i$ in the equation, requires an iterative numerical algorithm that is able to enforce the convergence. Here, the Newton-Raphson iterative procedure is used, which necessitates the linearization of (4.28) in terms of the guessed solution. For convenience, in ${}^k\widetilde{\mathbf{Y}}^i$ let the left superscript k denote $\widetilde{\mathbf{Y}}^i$ after k-th iteration within the Newton-Raphson loop. At each time step denoted by i, the solution vector $\widetilde{\mathbf{Y}}^i$ can be guessed through [39, 29, 64]:

$$
{}^k\widetilde{\mathbf{Y}}^i = {}^{k-1}\widetilde{\mathbf{Y}}^i - ({}^{k-1}\widetilde{\mathbf{J}}^i)^{-1}\left(\Xi_1{}^{k-1}\widetilde{\mathbf{Y}}^i + \Xi_2\widetilde{\mathbf{Y}}^{i-1} + \Xi_3\dot{\widetilde{\mathbf{Y}}}^{i-1} + (1-\beta_t){}^{k-1}\widetilde{\mathbf{F}}^i + (\beta_t)\widetilde{\mathbf{F}}^{i-1}\right)
\tag{4.29}
$$

In which $\mathbf{J}$ denotes the Jacobian matrix which is defined as

$$
{}^{k-1}\widetilde{\mathbf{J}}^i = (1-\beta_t)\frac{\partial\,{}^{k-1}\widetilde{\mathbf{F}}^i}{\partial\,{}^{k-1}\widetilde{\mathbf{Y}}^i} + \Xi_1
\tag{4.30}
$$

where the assembled matrix associated with $\frac{\partial\widetilde{\mathbf{F}}^i}{\partial\widetilde{\mathbf{Y}}^i}$ can be constructed by:

$$
\widetilde{\mathbf{F}}_{\mathbf{Y}^i} = \frac{\partial\,\widetilde{\mathbf{F}}^i}{\partial\widetilde{\mathbf{Y}}^i} =
\begin{bmatrix}
\mathbf{F}_{\mathbf{Y}_1^i} & \mathbf{F}_{\mathbf{Y}_2^i} & \mathbf{O} & \cdots & \mathbf{O} \\
\mathbf{O} & \mathbf{F}_{\mathbf{Y}_2^i} & \mathbf{F}_{\mathbf{Y}_3^i} & \mathbf{O} & \vdots \\
\vdots & \ddots & \ddots & \ddots & \mathbf{O} \\
\mathbf{O} & \cdots & \mathbf{O} & \mathbf{F}_{\mathbf{Y}_{N-1}^i} & \mathbf{F}_{\mathbf{Y}_N^i} \\
\mathbf{O} & \cdots & \cdots & \cdots & \mathbf{O}
\end{bmatrix}_{12N\times12N}
\tag{4.31}
$$

in which $\mathbf{F_Y}$ is defined through:

$$\mathbf{F_Y} = \begin{bmatrix} [\boldsymbol{\kappa}]_\times & [\boldsymbol{t}]_\times & -[\boldsymbol{v}]_\times & \mathbf{O} \\ \mathbf{O} & [\boldsymbol{\kappa}]_\times & -[\boldsymbol{\omega}]_\times & \mathbf{O} \\ \mathbf{O} & \mathbf{O} & -[\mathbf{B}\boldsymbol{\kappa}]_\times + [\boldsymbol{\kappa}]_\times\mathbf{B} & [\boldsymbol{t}]_\times \\ \mathbf{O} & \mathbf{O} & -[\boldsymbol{f}]_\times & [\boldsymbol{\kappa}]_\times \end{bmatrix}_{12\times12} \tag{4.32}$$

It should be noted that, the operator $[\,]_\times$ transforms a vector into the associated skew-symmetric matrix [32]. For instance, consider the velocity vector $\boldsymbol{v} \in \mathbb{R}^3$ given by $\boldsymbol{v} = (v_1, v_2, v_3)$ for which the corresponding skew-symmetric matrix $[\boldsymbol{v}]_\times \in \mathbb{R}^{3\times3}$ is found through

$$[\boldsymbol{v}]_\times = \begin{bmatrix} 0 & -v_3 & v_2 \\ v_3 & 0 & -v_1 \\ -v_2 & v_1 & 0 \end{bmatrix} \tag{4.33}$$

4.4   Post-processing Output

Once the differential equations were sufficiently integrated through time and the solution vector $\mathbf{Y}$ is found at each temporal step, we employ the method of *incremental rotation* to construct the transformation matrices through which the geometrical shape of the filament will be obtained [11, 29, 64]. In this method, the matrix exponential is used to capture the rotations of each cross-section through the space and time [3, 62, 36, 32]. Let $\mathbf{L}$ denote the transformation matrix and θ be the angle that represents the rotation about the unit vector axis , then we have:

$$\mathbf{L} = e^{([-\boldsymbol{\theta}]_\times)} \tag{4.34}$$

where $[.]_\times$ represents the skew-symmetric operator and $\boldsymbol{\theta}$ is defined :

$$\boldsymbol{\theta}_j^i = \frac{\Delta s}{2} \left(\boldsymbol{\kappa}_{j-1}^i + \boldsymbol{\kappa}_j^i \right) \tag{4.35}$$

We then obtain the exponential matrix using the Rodrigues formula [89, 32] and compute the transformation matrix $\mathbf{L}$ using the following formula:

$$\mathbf{L}_j^i = \text{expm} \left(-\boldsymbol{\theta}_j^i \right) \mathbf{L}_{j-1}^i \tag{4.36}$$

where *expm* represents the exponential matrix operator.

4.5   The Combined Elastohydrodynamic Model

To summarize the procedure for combining the computational rod model with SBT, we first review the two important equations provided in chapter 4 and 3 that respectively capture the structural dynamics of the filament and the nonlocal hydrodynamic

loading imposed by the surrounding fluid on the filament. Here, we rewrite the two important equations, the first of which is attributed to the SBT for the hydrodynamic analysis that first is defined in (3.5)

$$\boldsymbol{v}(s_q) = \mathbf{u}^\infty(s_q) + \left(\frac{1}{c_\perp}\boldsymbol{f}^h_\perp(s_q)\right) + \left(\frac{1}{c_\|}\boldsymbol{f}^h_\|(s_q)\right) +$$

$$\frac{\Delta s}{8\pi\mu}\Bigg[\sum_{j=1, j\neq i}^N \mathbf{G}^w(\mathbf{r}(s_q), \mathbf{r}_0(s_j), \mathbf{r}_0^{im}(s_j)) \cdot \boldsymbol{f}^h(s_j) + \tag{4.37}$$

$$\frac{-a}{2}\sum_{j=1, j\neq q}^N \mathbf{D}^w(\mathbf{r}(s_i), \mathbf{r}_0(s_j), \mathbf{r}_0^{im}(s_j)) \cdot \boldsymbol{f}^h_\perp(s_j)\Bigg]$$

where $1 \leq q, j \leq N$ in which N shows the number of cross-sections, and $\boldsymbol{f}^h$ denotes the hydrodynamic force exerted from the cross-section on the fluid. The second equation from (4.29) that through the 12×1 vector $\mathbf{Y} = (\boldsymbol{v}, \boldsymbol{\omega}, \boldsymbol{\kappa}, \boldsymbol{f})^T$ determines the four vector quantities namely linear velocity $\boldsymbol{v}$, angular velocity $\boldsymbol{\omega}$, curvature along the filament $\boldsymbol{\kappa}$, and the net internal force at each cross-section $\boldsymbol{f}$, at all spatial and temporal nodes:

$$^k\widetilde{\mathbf{Y}}^i = {}^{k-1}\widetilde{\mathbf{Y}}^i - \left({}^{k-1}\widetilde{\mathbf{J}}^i\right)^{-1}\left(\Xi_1\,{}^{k-1}\widetilde{\mathbf{Y}}^i + \Xi_2\widetilde{\mathbf{Y}}^{i-1} + \Xi_3\dot{\widetilde{\mathbf{Y}}}^{i-1} + (1-\beta_t)\,{}^{k-1}\widetilde{\mathbf{F}}^i + (\beta_t)\widetilde{\mathbf{F}}^{i-1}\right)$$

$$\tag{4.38}$$

where $\widetilde{\mathbf{Y}}^i = (\mathbf{Y}^i_1, \mathbf{Y}^i_2, \,...\,, \mathbf{Y}^i_N)^T$ holds $\mathbf{Y}$ at all nodes in space but at $t = i\,\Delta t$. Now, we follow the procedure in the following order:

1st: start by setting $i = 1$

2nd: use the known velocity of cross-sections $\boldsymbol{v}$ obtained from the previous time step then invert the equation (4.37) as explained in chapter 3, to compute the hydro-dynamic forces $\boldsymbol{f}^h$ at all spatial nodes

3rd: update the vector of non-homogeneous terms $\widetilde{\mathbf{F}}^{i-1}$ simply by substituting $\boldsymbol{f}^{ext} = -\boldsymbol{f}^h$ inside of each $\mathbf{F}^{i-1}_j$

4th: start the Newton-Raphson iterations beginning with $k = 1$

5th: update the vector of non-homogeneous terms ${}^{k-1}\widetilde{\mathbf{F}}^i$ using the known information at ${}^{k-1}\widetilde{\mathbf{Y}}^i$

6th: iterate equation (4.38) by setting $k = k+1$ until the convergence is guaranteed

7th: set $i = i + 1$ and start over to determine the solution in the Next time step

Chapter 5

Accuracy of the Slender Body Theory compared to CFD and Local Hydrodynamic models

Here in this chapter, we consider multiple case studies to examine the range in which Slender Body Theory (SBT) provides a reliable solution for the hydrodynamic loads exerted on the filament. It is important to mention again that all the simulations in this thesis and more specifically this chapter, are conducted for filaments that move at low Reynolds numbers where inertial forces of fluid are very small compared to the viscous forces in the Navier-Stokes equations. This reduces the nonlinear Navier-Stokes differential equations into the linear Stokes equations where the solution is mathematically obtainable. SBT takes advantage of the linearity of the Stokes equations and employs the singularity solutions discussed in detail in chapter 2 and 3 to determine the velocity and pressure field in the domain of interest around the slender filament. In essence, the theory provides an exact solution when the slenderness ratio of the filament, which is the length over the radius ratio, is infinitely large. Typically the range in which slender objects such as Carbon Nanotubes (CNTs) and flagellar filaments exist, the slenderness ratio is found to be in the order of $\sim O(10)$ to $\sim (1000)$. Therefore, it would be worth investigating the accuracy of the SBT and estimate the error at different slenderness ratio values. A Computational Fluid Dynamic (CFD) solver would indeed be a reliable benchmark, which can provide a reasonably accurate solution to the fluid flow around the corresponding slender objects. Here, we used COMSOL Multiphysics® v. 5.3 as our finite element CFD solver and compared the results with SBT. In some case studies, rather than the SBT and CFD solutions, we include the lower order SBT solutions, namely, the Resistive Force Theory (RFT) and the Wall-Resistive Force Theory (W-RFT). The resistive forces or local hydrodynamic solutions are the most basic solutions of SBT that neglect higher-order nonlocal terms in the integral formulations of SBT resulting in the leading-order terms be the only contributors to the hydrodynamic drag force. More

specifically, the RFT solutions provide a linear relationship between the local velocity of each segment of the filament and the hydrodynamic drag force imposed by the nearby fluid. The RFT solutions indeed will not account for the nonlocal interactions arising from the incompressibility of the fluid and therefore is accompanied by more error when the filament is highly curved or surrounded by other no-slip bounderies[23].

In the following sections of this chapter, the CFD simulations are involved and the total hydrodynamic drag forces on each filament are compared with the local and nonlocal hydrodynamic models. In three different scenarios of a filament in an unbounded domain, in the proximity of a no-slip infinite plane wall, and attached to a no-slip plane wall, we investigate the total drag force exerted on each filament. We then compare the results of our slender body formulations with those obtained by Pozrikidis (2011) in [81], where the hydrodynamic forces per unit arc-length are computed for three rods of different slenderness ratios attached to a no-slip wall. Let us again review the abbreviations used throughout this chapter of the thesis:

- CFD (Computational Fluid Dynamics): Results of hydrodynamic loads on a slender cylinder obtained from the COMSOL Multiphysics® v. 5.3 as our CFD solver

- SBT (Slender Body Theory): Results of the hydrodynamic loads on an unbounded cylindrical filament, obtained from our computational model solved via MATLAB® v. R2018b [81, 23]

- W-SBT (Wall-Slender Body Theory): Results of the hydrodynamic loads on a cylindrical filament bounded by a no-slip wall, obtained from our computational model solved via MATLAB® v. R2018b [8, 9, 45]

- RFT (Resistive Force Theory): The leading-order hydrodynamic loads on an unbounded cylindrical filament obtained from SBT formulations [96, 20]

- W-RFT (Wall-Resistive Force Theory): The leading-order hydrodynamic loads on a cylindrical filament bounded by a no-slip wall obtained from W-SBT [12]

Figure 5.1: Schematic of the cylinder close to the no-slip wall

In addition to the short forms of the most used definitions discussed above, FIG. 5.1 introduces the cylinder by its radius a and length L where the slenderness ratio is defined by $\eta = L/a = \varepsilon^{-1}$ (in chapter 2 we employed ε to represent the slenderness ratio but in this chapter it would be more convenient to work with η the length-over-radius ratio). For the case of a filament moving in the proximity of a no-slip plane wall, the gap between the center-line of the filament and the rigid wall is defined by h. The following properties for the fluid are considered; $\mu[pa.s]$ is the dynamic viscosity, $\rho[kg.m^{-3}]$ is the density of the fluid, $\mathbf{u}^{\infty}[m.s^{-1}]$ represents the velocity of the fluid in far-field while $\mathbf{V}[m.s^{-1}]$ denotes the velocity assigned to the stokeslets. For more realistic choice of parameters, we take the example of primary cilia [90] moving in liquid water. The length of the filament is chosen to be $L = 10^{-6}[m]$, so that the change in radius a, defines the slenderness ratio of the filament η. Moreover, the viscosity $\mu = 10^{-3}[pa.s]$ and density $\rho = 10^{3}[kg.m^{-3}]$ represent the properties of liquid water. Typically the values assigned to the far-field velocity of the fluid or the velocity of the stokeslets are in the order of $O(10^{-3}[m.s^{-1}])$. Therefore the maximum Reynolds' number $Re = \rho V D/\mu$ for the fluid passing around the filaments will be found in $\sim O(10^{-4})$ or smaller, which ensures that the Stokes' flow equations govern the motion of the fluid. Although, we choose dimensional parameters that can represent a physical system, but we will report all the results using nondimensionalized values.

5.1 Flow Passing An Unbounded Sphere

To understand the error associated with the CFD simulations, we first study two cases where the fluid passes a sphere with the Reynolds' numbers of $Re = 0.001$ and $Re = 0.002$ corresponding to the diameters of $D = 1[\mu m]$ and $D = 2[\mu m]$, respectively. The advantage to such a case study is that the total drag force computed

by the CFD simulations can directly be compared to its theoretical value known as the *Stokes's law*:

$$F = 3\pi D\mu V \tag{5.1}$$

to measure the error associated with each choice of mesh size in the computational domain. Meshing in COMSOL is mainly associated with multiple built-in tools that provide users with more flexibility and functionality. In our CFD simulations, we have considered two separate meshing domains; the first is attributed to the sphere for which the total drag force will be calculated, and the next is the domain in which the fluid flows. To maintain the accuracy of the CFD results with the least computational costs, a spatial adaptive mesh is applied to the computational domain. Since the CFD solution is of higher importance in the proximity of the sphere, a very fine mesh size is assigned to the boundary of the sphere and coarser mesh size to the fluid domain. This mesh refinement technique will ensure that the elements closer to the sphere have the least mesh sizes but they gradually shift toward coarser meshes as they move away from the sphere boundary. To control the meshing parameters in COMSOL, we use the *extremely fine mesh size* for the sphere with manually adjustable values for the *maximum mesh size*, along with the *fine mesh size* for the fluid domain. As a result, both spheres with mesh sizes of 0.05, 0.075, 0.1, 0.2,and 0.5 meters (see FIG. 5.2 and FIG. 5.3) are placed in the middle of a sufficiently large channel where the fluid with $\mathbf{u}^\infty = (1, 0, 0)[mm.s^{-1}]$ flows around the sphere. The theoretical values suggest that the total drag force on the sphere with $D = 1[\mu m]$ and $D = 2[\mu m]$ should respectively match $F_1 = 9.424[pN]$ and $F_2 = 18.849[pN]$.
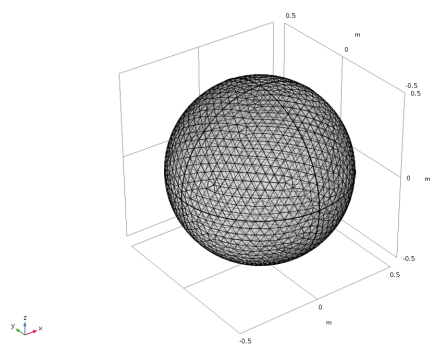
(a) Max Mesh Size = 0.050
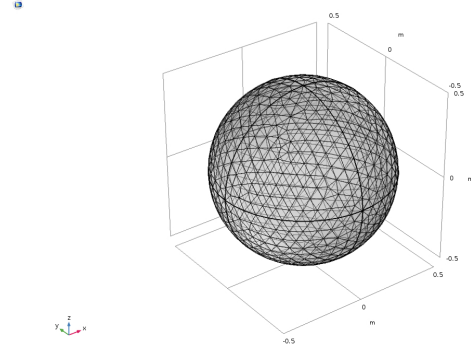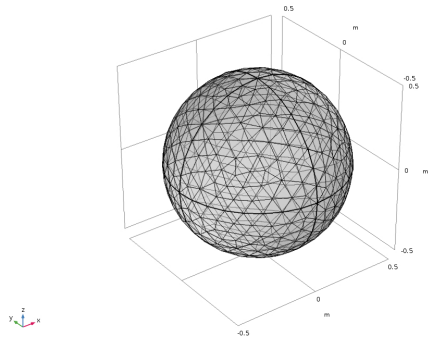
(b) Max Mesh Size = 0.075
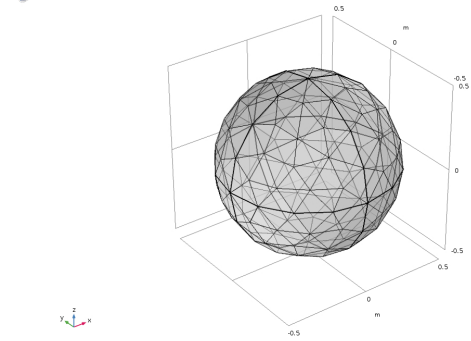
(c) Max Mesh Size = 0.1
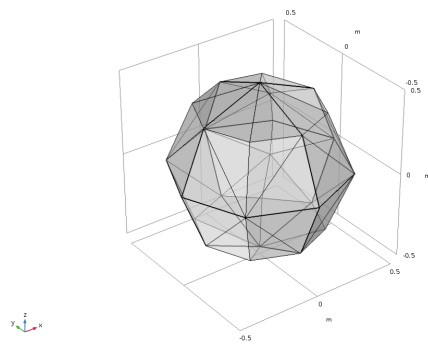
(d) Max Mesh Size = 0.2

(e) Max Mesh Size = 0.5

Figure 5.2: Different mesh sizes on a sphere with $D = 1[\mu m]$ (all values in micron-meters)

(a) Max Mesh Size = 0.050
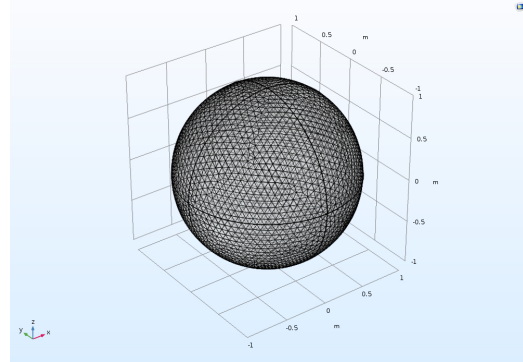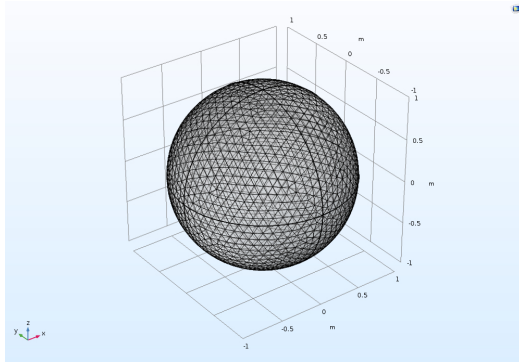
(b) Max Mesh Size = 0.075
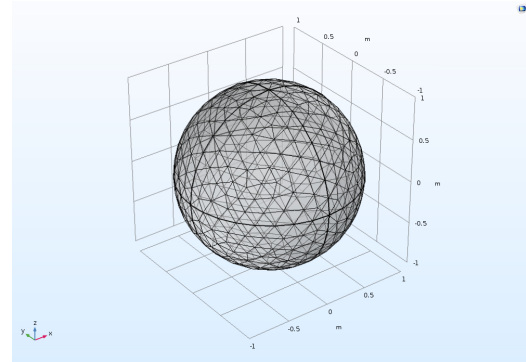
(c) Max Mesh Size = 0.1
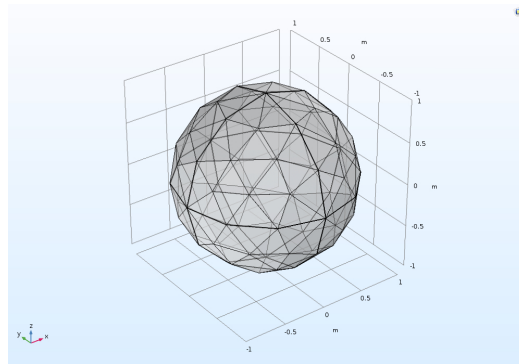
(d) Max Mesh Size = 0.2

(e) Max Mesh Size = 0.5

Figure 5.3: Different mesh sizes on a sphere with $D = 2[\mu m]$ (all values in micrometers)

As is shown in FIG. 5.4, the results suggest that the error has been reduced to $\sim 0.2\%$ for the sphere with $D = 2[\mu m]$ and $\sim 2.6\%$ for the sphere with $D = 1[\mu m]$ when the max mesh size is kept $0.05[\mu m]$. Typically the error below the 5% is considered to be reasonable for our CFD simulations. We should also note that the flow past the filaments with higher slenderness ratios, may require more mesh refinements and smaller mesh sizes. In the 3D simulations in COMSOL, meshing the objects with aspect-ratios (length over the radius) more than 100 should be avoided since solving the resulting system of equations would become harder as the aspect ratio increases[103]. Therefore, errors associated with a high slenderness ratio obtained by our CFD simulations are inevitable but with some mesh refinement techniques at higher aspect ratios we kept the error around or below 5%. The sphere case studies helped us understand the range in which the error lies below the 5%. Last but not least, in the whole CFD simulations in this chapter, a *fully-coupled stationary solver* (also referred to as the steady-state solver) with tolerance set to 0.001 is used. For further information about the solver and the termination criteria, the reader is referred to [47].
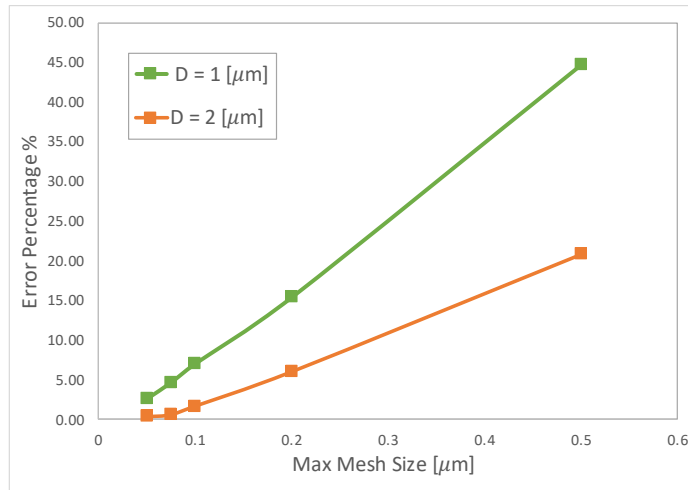
Figure 5.4: Error analysis for the total drag force computed by the CFD simulations compared to the theoretical values obtained from the Stokes' drag force on the sphere.

5.2 Total Hydrodynamic Force on a Free-Free Filament in Unbounded Flow

The total hydrodynamic drag load on a filament moving in an unbounded domain, away from any other rigid boundary is evaluated at different slenderness ratios. In

these simulations, the rod is moving with $V = 1 \ [mm.s^{-1}]$ in the Z direction and perpendicular to its central X-axis. Note that the fluid around the rod is initially at rest and all the disturbances in the fluid domain are produced by the motion of the filament after the movement. In FIG. 5.5 the velocity contours and streamlines for the filament with $\eta = 50$ are illustrated. Next in the FIG. 5.6, the total hydrodynamic force on each filament versus their slenderness ratios of $\eta = 20, 30, 40, 50, 75$, and 100 using the SBT, RFT, and CFD methods are determined and the difference percentage with respect to the SBT is reported.

(a) Velocity Contours   (b) Velocity Streamlines
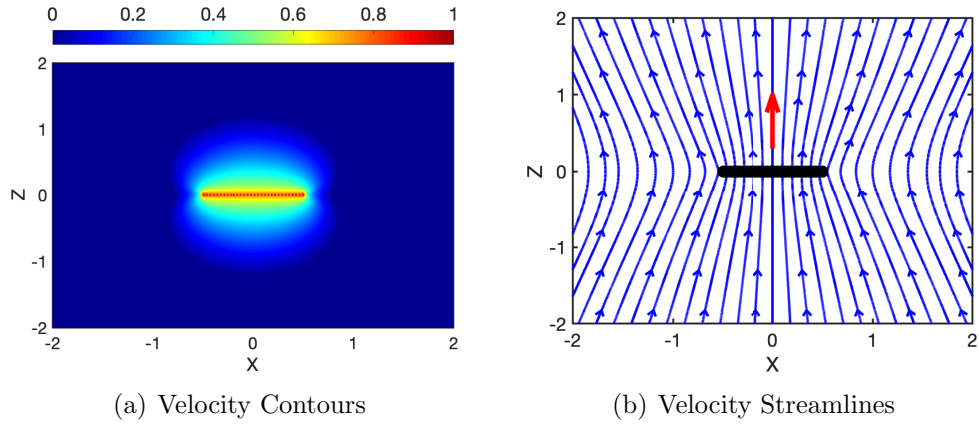
Figure 5.5: *SBT for an unbounded slender filament in Stokes flow*: The velocity field around a slender rod of $\eta = 50$ using SBT is demonstrated. Here, a straight slender filament with velocity $V = 1[mm.s^{-1}]$ which is immersed in a fluid with $\mu = 10^{-3}[pa.s]$, is moving perpendicular to its x-axis. The simulations are in 3D but here we have only illustrated the solutions on a 2D XZ-plane that cuts across the symmetry axis of the Cylinder.

The FIG. 5.6 (a), shows a logarithmic reduction in the drag force as the slenderness increases. The reason for the logarithmic decrease of the drag can readily be verified by looking at the lowest order drag force approximation equation (3.12) in which the drag force is proportional to $1/\ln(\eta)$. The FIG. 5.6 (b) also implies that the reduction in the difference percentage is achievable with the increase in the slenderness ratio. A quantitative analysis on the same figure suggests that at the lowest slenderness ratio $\eta = 20$, SBT predicts 6.5% difference compared to the CFD results while at the highest slenderness ratio $\eta = 100$ it has been reduced to less than 2%. The SBT versus RFT comparisons signifies that the difference is $\sim 1\%$ for $\eta = 20$ but drops to $\sim 0.5\%$ for higher slenderness ratios.

(a) Total Drag Force   (b) Difference Between Methods

Figure 5.6: (Left)The total non-dimensionalized hydrodynamic drag force on slender filaments of different slenderness ratios η are computed using SBT, CFD, and RFT. (Right) The difference percentage associated with the SBT compared to RFT and CFD are shown in the graph.

5.3   Total Hydrodynamic Force on a Free-Free Filament Moving in Proximity of a No-slip Plane Wall

As discussed thoroughly in chapter 2 and 3, the presence of any boundary in the proximity of the singularity solutions, imposes another boundary condition to the system of equations that needs to be satisfied in the final solution. Here, the singularity solutions that are distributed along the center-line of the filament, are moving close to a rigid plane wall located at $Z = 0$ with no-slip boundary condition on its surface. Thus, we need to employ the image singularities $\mathbf{G}^w$ and $\mathbf{D}^w$ and use the equation (3.4) which unconditionally satisfies the no-slip boundary condition on the surface of the plane wall. In this problem the filament is located on top of the wall with the gap distance $h = 0.2[\mu m]$ and is moving with velocity $V = 1[mm.s^{-1}]$ in the Z direction (see FIG. 5.3). The fluid is initially at rest thus $\mathbf{u}^\infty = (0, 0, 0)$ anywhere before the movement of the rod is initiated. As a result, we determine the total hydrodynamic drag force on filaments with slenderness ratios of $\eta = 20, 30, 40, 50,$ and 75 using W-SBT, CFD, and W-RFT and demonstrate them on FIG. 5.8.

(a) Velocity Contours

(b) Velocity Streamlines
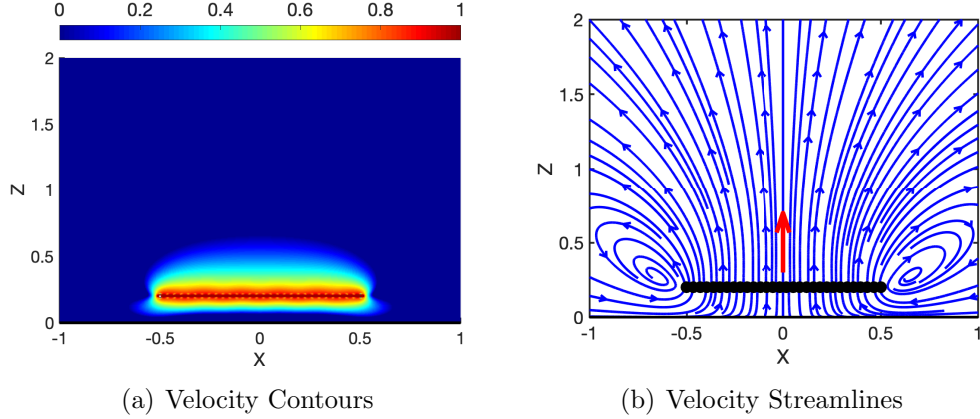
Figure 5.7: *W-SBT for a slender filament moving near a rigid plane wall (Z=0) at low Reynolds' number*: The velocity field around a slender rod of $\eta = 50$ using W-SBT is demonstrated. Here, a straight slender filament with velocity $V = 1[mm.s^{-1}]$ which is immersed in a fluid with $\mu = 10^{-3}[pa.s]$, is moving away from the plane wall. The simulations are in 3D but here we have only illustrated the solutions on a 2D XZ-plane that cuts across the symmetry axis of the Cylinder.

Similar to the unbounded filament scenario, a logarithmic reduction in the difference percentage is expected from our current case in which the filament is moving near a wall. This logarithmic behaviour can also be verified by looking at the W-RFT formulations provided by [12]:

$$\xi_z^w = 2\xi_x^w = \frac{4\pi\mu}{\ln\left(\frac{2h}{a}\right)}, \quad \xi_y^w = \frac{4\pi\mu}{\ln\left(\frac{2h}{a} - 1\right)} \quad \text{if} \quad h \ll L \tag{5.2}$$

$$\xi_z^w = \frac{4\pi\mu}{\ln(\eta) + 0.193 - \frac{3L}{4h}}, \quad \xi_x^w = \frac{2\pi\mu}{\ln(\eta) - 0.807 - \frac{3L}{16h}},$$
$$\xi_y^w = \frac{4\pi\mu}{\ln(\eta) + 0.193 - \frac{3L}{8h}}, \quad \text{if} \quad h \gg L \tag{5.3}$$

In this case ξ_x^w, ξ_y^w, and ξ_z^w are the drag coefficients along the X,Y, and Z directions, respectively (see FIG. 5.1). As the equation (5.2) suggests, in the limiting case of $h/L \ll 1$ the drag force becomes proportional to $1/ln(2h/a)$. It would indeed be true that in (5.2) the h/a determines the value of the drag coefficient but it is also worth mentioning again that in our simulations L and h are kept constant so that any change in the radius of the filament affects both the slenderness $\eta = L/a$ as well as the h/a ratio. Therefore at a constant h/L ratio, a decrease in the slenderness ratio would result in a logarithmic decrease in the drag force. However, we would expect

that the W-RFT hydrodynamic drag coefficients converge to those predicted by RFT as the body is relatively far away from the wall. We can readily verify this statement by considering the equation (5.3), since the L/h ratio vanishes when the filament is relatively far from the wall.

An important result that can be interpreted from the FIG. 5.3 is that in the near-wall swimming scenario, the total hydrodynamic drag force exerted on each filament is about two to three times higher than the drag force on the same filaments but in the unbounded domain. Therefore, the closer a filament or micro-swimmer to a wall is, the harder the motion will be and the higher energy is required to overcome the hydrodynamic viscous forces. The drag however logarithmically decreases as either the distance between the filament and the wall is reduced or the slenderness ratio is increased.

(a) Total Drag Force   (b) Difference Between Methods
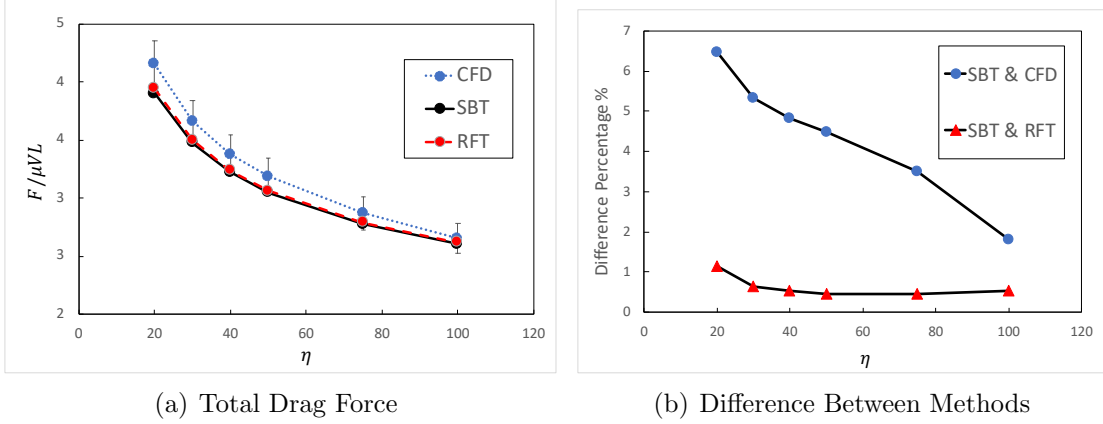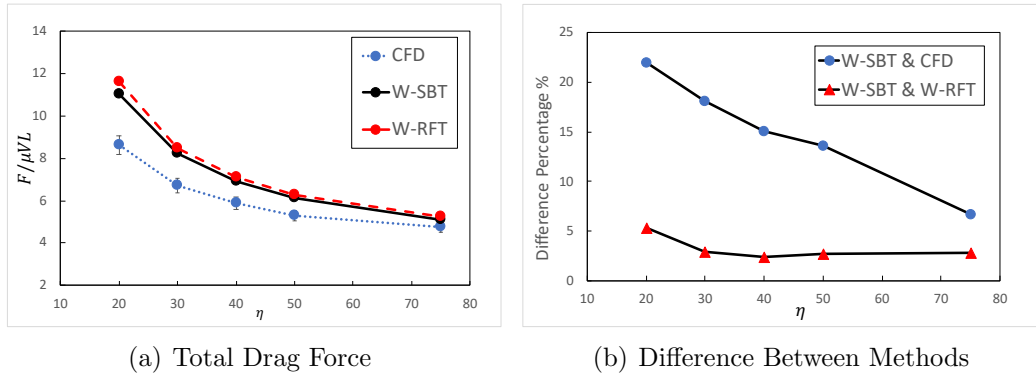
Figure 5.8: (Left)The total non-dimensionalized hydrodynamic drag force on slender filaments of different slenderness ratios η moving close to a rigid wall are computed using W-SBT, CFD, and W-RFT. (Right) The difference percentage associated with the W-SBT compared to W-RFT and CFD are shown in this graph

Not only the drag compared to the unbounded motion is increased but also the difference percentage between the W-SBT and the CFD is increased. There are a few reasons for this matter that needs to be discussed. Fundamentally, W-SBT replaces the center-line of the filament with the appropriate singularity solutions of the Stokes flow and determines the strength of the potential dipoles (see equation 3.3) with the zero error at infinite slenderness ratio [63]. Indeed the error increases as the radius increases but in the near-wall filament scenario with the example of $h = 0.2$ the radius can not exceed the gap distance h since it would collide with the wall at $a = 0.2$. Here, in the case of $\eta = 20$ the radius of the filament is $a = 0.05$. This means that the filament has already filled 25% of the gap under the filament, and the fluid can only flow in the remaining 75% (imagine an XZ plane cutting across the center-line

of the filament). This fact itself can violate the premise of W-SBT and W-RFT where the $h/L \ll 1$ but $a/h \sim O(1)$. In such cases, the slender-body, as well as the resistive-force formulations, need to be reformulated considering the a/h ratio otherwise it would be better to avoid the high a/h values. As a result, we observe that the difference percentage between W-SBT and CFD is dropped from $\sim 22.5\%$ to $\sim 7\%$ for slenderness ratios of $\eta = 20$ and $\eta = 75$, respectively. The predicted drag forces associated with the W-SBT and W-RFT results are relatively in good agreement at slenderness ratios of higher than $\eta = 20$ where the difference percentage is about 2%.

5.4 Hydrodynamic Forces on a Fixed-Free Filament Attached to a No-slip plane Wall

5.4.1 Hydrodynamic Force per unit arc-length

Using our W-SBT model, we have obtained the distribution of the hydrodynamic forces along the center-line of a filament attached to a no-slip plane wall, which is subjected to shear flow at far-field. Then, the results are qualitatively compared with those obtained by Pozrikidis in [81]. FIG. 5.4.1 suggests that our SBT simulations are in a good agreement with Pozrikidis[81] where f_z (our SBT) or b_y (by [81]) represent the force per unit arc-length of the rod distributed along the vertical axis or the center-line of the rod. However, our results show that there are some oscillations near the endpoints of the filament. The *endpoint effect* was first observed by Cortez in 2018 [16] and is also well-discussed in [102] section 2.5. In our SBT model, the endpoint effect typically encompasses the last 3 points near the two tips, such that the force on the second-last cross-section indicates a non-monotonic behavior. This may have a trivial effect on the computation of the total drag force on the filament, which is the main focus of this chapter. It is also worth mentioning that as the slenderness ratio increases the endpoint effect vanishes and the monotonic response is achievable.

(a)   (b)
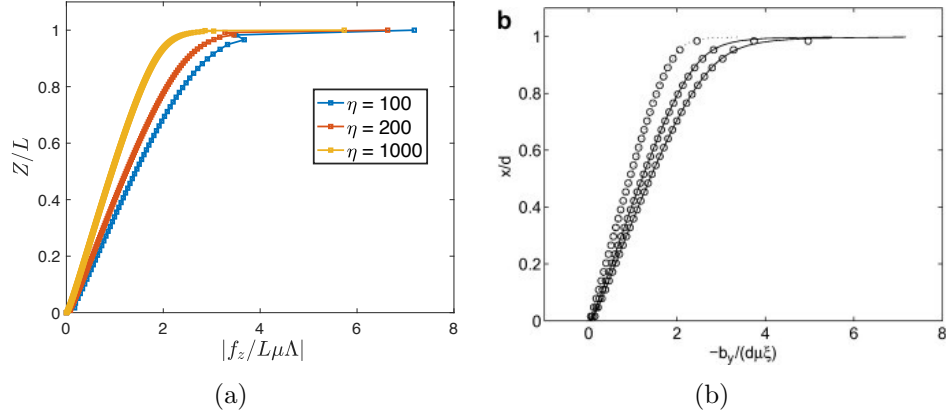
Figure 5.9: (a) Our SBT simulations (b) Results obtained by Pozrikidis[81] Reused by permission from Elsevier Ltd. under the license number 4942111488997

5.4.2 Total Hydrodynamic Force on the filament

SBT and W-SBT are not only able to determine the flow around a moving filament which is immersed in a fluid at rest with $\mathbf{u}^\infty = (0,0,0)$ anywhere but also can capture the disturbances produced by a slender filament subjected to an incoming flow with an arbitrary profile of $\mathbf{u}^\infty(X,Y,Z)$ at far-field. Thanks to the linearity of the Stokes equations, a superposition of the aforementioned problems is also feasible. Here in the FIG. 5.10, a slender filament with $\eta = 50$ is attached to a no-slip plane wall and is subjected to a shear flow (also referred to as the *Couette flow*) with the profile $\mathbf{u}^\infty = (0,0,\Lambda Z)[mm.s^{-1}]$ at far-field. In the FIG. 5.4.2 the satisfaction of the no-slip boundary condition on both the surface of the plane wall and the filament is observable which translates into zero velocity on the boundaries.

(a) Velocity Contours

(b) Velocity Streamlines

(c)
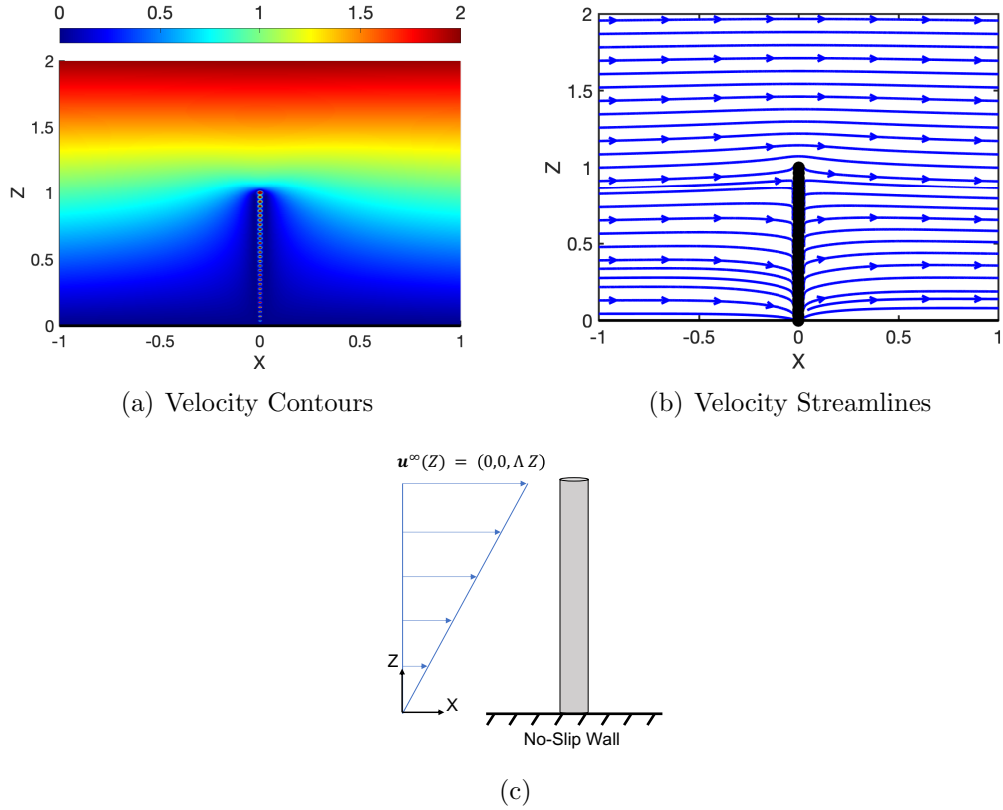
Figure 5.10: *W-SBT results for a slender filament attached to a rigid plane wall at located Z=0*: The velocity field around a slender rod of $\eta = 50$ using W-SBT is demonstrated. Here, a straight slender filament is subjected to a shear flow with $\mathbf{u}^\infty = (0, 0, \Lambda Z)[mm.s^{-1}]$ and viscosity $\mu = 10^{-3}[pa.s]$. The simulations are in 3D but here we have only illustrated the solutions on a 2D XZ-plane that cuts across the symmetry axis of the Cylinder.

Using CFD and W-SBT, we have obtained the total hydrodynamic drag forces exerted on the filaments with slenderness ratios of $\eta = 20, 30, 40, 50, 75$ and 100. As expected, the hydrodynamic force on the filament logarithmically decreases as the slenderness ratio increases. In the CFD simulations, with the presence of a no-slip wall, the velocity profile defined at the inlet will no longer match the velocity profile obtained in the proximity of the wall. Therefore, we chose the size of the channel to be much larger than the size of the filament so that the fully developed velocity profile that reaches the filament is linear. This way a reasonable comparison between the W-SBT and the CFD simulations can be made. As could be expected, the quantitative analysis of the results shown by FIG. 5.4.2 suggests that the total force decreases

56

with the increase in the slenderness ratio in a logarithmic manner. The difference percentage range is between $\sim 8.1\%$ and $\sim 6.9\%$ for the slenderness ratios between $\eta = 20$ and 100, respectively.

(a) Total Drag Force   (b) Difference Between Methods
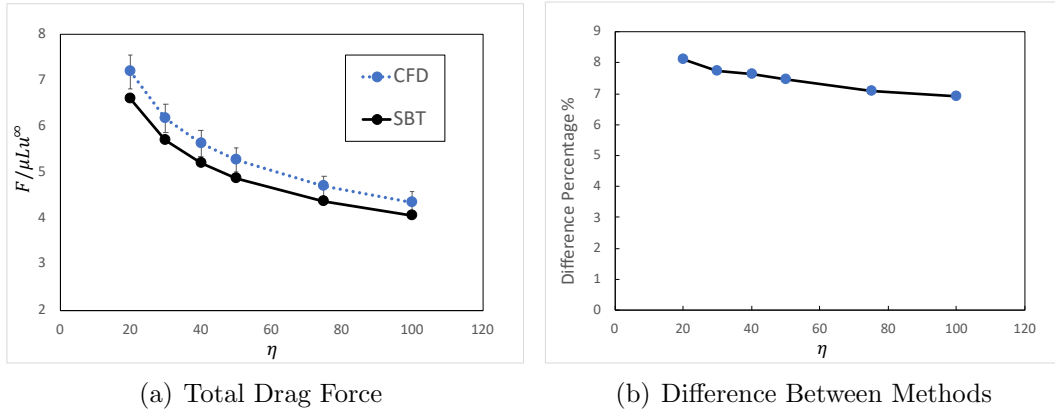
Figure 5.11: *W-SBT for a slender filament attached to a rigid plane wall located at Z=0 :* The fluid velocity field around a slender rod of $\eta = 50$ using W-SBT is demonstrated. Here, a straight slender filament is subjected to a shear flow with $\mathbf{u}^\infty = (0, 0, \Lambda Z)[mm.s^{-1}]$, $\Lambda = 2.57 * 10^6[s^{-1}]$. The simulations are obtained in 3D but here we have only illustrated the solutions on a 2D XZ-plane that cuts across the symmetry axis of the Cylinder.

Chapter 6

Fluid-Structure Interaction Analysis of Slender Elastic Biological Filaments

6.1 Summary

Mimicking the beating pattern of elastic biological filaments such as flagella and cilia in a dissipative viscous liquid at low Reynolds numbers requires a robust computational model that can both capture the dynamics of a buckled filament as well as full hydrodynamics between the structure and the fluid. At low Reynolds numbers or namely, "Stokes Regime" viscous forces are dominant over inertial forces resulting in a linear relationship between the drag force and velocity. To solve such elastohydrodynamic problem, the *Computational Rod Model* which captures the structural dynamics of an elastic filament is combined with *Slender Body Theory* that captures the hydrodynamic interactions of the filament with fluid to compute the rod deflections at each time step. Using an iterative procedure with the initial and boundary conditions appropriate to the problem at hand the hydrodynamic drag forces on a fixed-free filament attached to a rigid wall is computed and the subsequent shapes obtained.

6.2 Model and Formulations

Slender Body Theory: The Green's function for the Stokes equations in the presence of a singularity, referred to as a *"Stokeslet"*, is the fundamental solution to the Stokes equations. Mathematically the singularity or point force in Stokes equations can be represented by a Delta function. Equation (6.1) represents the Stokes equations where μ is the fluid viscosity, p is the pressure, $\mathbf{u}$ is the fluid velocity, $\mathbf{r}$ defines the position of any point in 3-dimensional space and $\mathbf{r}_0$ defines the position where the Stokeslet is

located, both taken relative to the inertial reference frame fixed at the origin. Here, δ is the Dirac delta function, and $\mathbf{F}\delta(\mathbf{r} - \mathbf{r}_0)$ represents a point force with strength $\mathbf{F}$ acting on the fluid at $\mathbf{r} = \mathbf{r}_0$. Equation (6.2) represents the Green's function $\mathbf{G}(\mathbf{r}, \mathbf{r}_0)$ for the Stokes flow in an unbounded fluid where $\mathbf{I}$ is the 3-by-3 identity matrix. The solution for the velocity field $\mathbf{u}$ that satisfies (6.1) and the boundary conditions is given by (6.3):

$$-\boldsymbol{\nabla} p + \mu \boldsymbol{\nabla}^2 \mathbf{u} = -\mathbf{F}\delta(\mathbf{r} - \mathbf{r}_0) \quad , \quad \boldsymbol{\nabla} \cdot \mathbf{u} = \mathbf{0}$$
$$\mathbf{u} \to \mathbf{u}_\infty \quad and \quad p \to p_\infty \quad as \quad \mathbf{r} \to \infty \tag{6.1}$$

$$\mathbf{G}(\mathbf{r}, \mathbf{r}_0) = \frac{1}{8\pi\mu} \left(\frac{\mathbf{I}}{|\mathbf{r} - \mathbf{r}_0|} + \frac{(\mathbf{r} - \mathbf{r}_0)(\mathbf{r} - \mathbf{r}_0)}{|\mathbf{r} - \mathbf{r}_0|^3} \right) \tag{6.2}$$

$$\mathbf{u}(\mathbf{r}) = \mathbf{G}(\mathbf{r}, \mathbf{r}_0) \cdot \mathbf{F} \tag{6.3}$$

In Slender Body Theory(SBT), the key idea is that the Stokeslets of unknown force strength can be distributed along the center-line of the filament. To evaluate the strength and direction of the force at each cross-section, the no-slip boundary condition which states the velocity of each cross-section should match the summation of induced fluid velocities by the rest of the Stokeslets at that material point should be satisfied. Thanks to the linearity of the Stokes equations, the velocity field around the filament can be directly obtained at an arbitrary point in the fluid as:

$$\mathbf{u}(\mathbf{r}) = \mathbf{u}_\infty(\mathbf{r}) + \frac{1}{8\pi\mu} \int_0^l \mathbf{G}(\mathbf{r}, \mathbf{r}_0(s)) \cdot \mathbf{F}(s)ds + \frac{1}{4\pi} \int_0^l \mathbf{D}(\mathbf{r}, \mathbf{r}_0(s)) \cdot \mathbf{d}(s)ds \tag{6.4}$$

$$\mathbf{D}(\mathbf{r}, \mathbf{r}_0) = \frac{1}{4\pi} \left(-\frac{\mathbf{I}}{|\mathbf{r} - \mathbf{r}_0|^3} + 3\frac{(\mathbf{r} - \mathbf{r}_0)(\mathbf{r} - \mathbf{r}_0)}{|\mathbf{r} - \mathbf{r}_0|^5} \right) \tag{6.5}$$

Here, in (6.4) s is the arc length along the center-line, l is the length of the filament, and $\mathbf{D}$ is the potential dipole with strength $\mathbf{d}$. The effect of the second integral in equation (6.4) is negligible [81, 80] due to the fast decay of the dipole with distance from each evaluation point at $\mathbf{r}_0$. Blake [8, 9] used the method of images to satisfy the no-slip boundary condition on the surface of a rigid wall where the flow is induced by a Stokeslet placed at a distance h from the wall, and derived the appropriate Green's function $\mathbf{G}^w(\mathbf{r}, \mathbf{r}_0(s))$ for a point force in the presence of a rigid wall. Neglecting the effect of dipoles and by replacing $\mathbf{G}(\mathbf{r}, \mathbf{r}_0(s))$ with $\mathbf{G}^w(\mathbf{r}, \mathbf{r}_0(s))$ in equation (6.4) the fluid velocity field near the filament will be determined.

Computational Rod Model: The continuum rod formulations that we use to track the elastic deformations of a flexible filament, follows the classical approach of Kirch-

hoff, which assumes each cross-section of the rod to be rigid. Equations of equilibrium (6.6) and (6.7), and equations of compatibility (6.8) and (6.9) are given below:

$$m(\frac{\partial \boldsymbol{\nu}}{\partial t} + \boldsymbol{\omega} \times \boldsymbol{\nu}) - (\frac{\partial \mathbf{f}}{\partial s} + \boldsymbol{\kappa} \times \mathbf{f}) - \mathbf{f}_e = \mathbf{0} \tag{6.6}$$

$$\mathbf{I}_m \frac{\partial \boldsymbol{\omega}}{\partial t} + \boldsymbol{\omega} \times \mathbf{I}_m \boldsymbol{\omega} - (\frac{\partial \mathbf{q}}{\partial s} + \boldsymbol{\kappa} \times \mathbf{q}) + \mathbf{f} \times \mathbf{r}_a - \mathbf{q}_e = \mathbf{0} \tag{6.7}$$

$$\frac{\partial \mathbf{r}}{\partial t} + \boldsymbol{\omega} \times \mathbf{r}_a - (\frac{\partial \boldsymbol{\nu}}{\partial s} + \boldsymbol{\kappa} \times \boldsymbol{\nu}) = \mathbf{0} \tag{6.8}$$

$$\frac{\partial \boldsymbol{\kappa}}{\partial t} - (\frac{\partial \boldsymbol{\omega}}{\partial s} + \boldsymbol{\kappa} \times \boldsymbol{\omega}) = \mathbf{0} \tag{6.9}$$

in which t is time, s is the arc length along the center-line, m is the mass per unit length of the rod, $\mathbf{I}_m$ is the 3 by 3 tensor of moment of inertia per unit length. The special derivative of vector $\mathbf{r}_0(s,t)$ with respect to s is denoted by the vector $\mathbf{r}_a$, vectors $\boldsymbol{\nu}(s,t)$ and $\boldsymbol{\omega}(s,t)$ capture the linear and angular velocity of cross-sections respectively, $\boldsymbol{\kappa}(s,t)$ represents the curvature, and the net internal force and internal moment over each cross-section of the rod are shown by vectors $\mathbf{f}(s,t)$ and $\mathbf{q}(s,t)$ respectively. The constitutive law with an algebraic form of $\mathbf{q}(s,t) = \mathbf{B}(s)\boldsymbol{\kappa}(s,t)$ is used where the matrix $\mathbf{B}$ encodes the bending and torsional stiffness moduli of the rod. External forces and moments imposed on cross-sections are captured by vectors $\mathbf{f}_e(s,t)$ and $\mathbf{q}_e(s,t)$ respectively. In our combined model, fluid drag forces computed by Slender Body Theory and follower forces distributed along the filament, communicate with Computational Rod Model through the vector $\mathbf{f}_e$. Nonlinear Equations (6.6)-(6.9), are integrated over time and space using the well-known generalized-α method discussed extensively in [29, 28, 27] and literature cited therein.
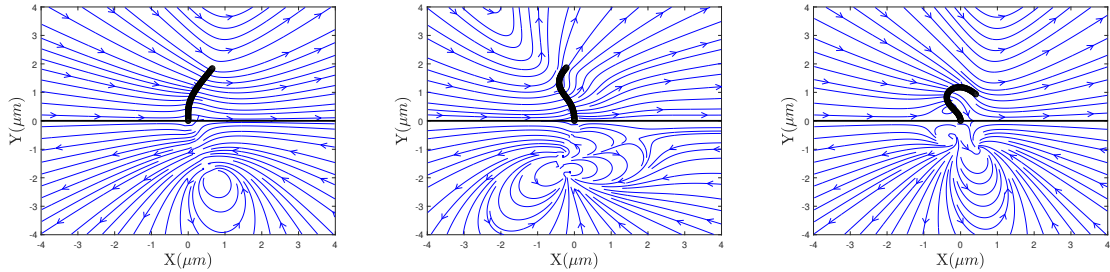
Figure 6.1: Initially, at time zero the filament is vertically straight. Buckling instabilities begin due to the effect of non-conservative follower forces which are distributed loads oriented tangentially to the deflection curve of the filament. Here, streamlines of velocity around a filament with Stokeslets distributed along the center-line, as well as the shape of the filament for three sequences of time are demonstrated. However, the bottom parts of the black line in the middle of the figures which demonstrate the presence of a solid wall, don't have any physical meaning but mathematically represent the contribution of image Stokeslets and image doublets to the fundamental solution of the Stokes flow. In this case, a filament with length of $l = 2\mu m$, slenderness ratio of 40 and elastic modulus $E = 3.06 \times 10^6 Pa$, immersed in a fluid of viscosity $\mu = 0.001 Pa.s$ with Re $\ll 0$ and subjected to follower forces of 65 pN/m is simulated. (Left) filament at time = 0.002s (Middle) filament at time = 0.007s (Right) filament at time = 0.015s

6.3   Results and Conclusion

Using the formulation presented here, we first derive the frequency-force relationship of planar oscillations for a slender micro-scale filament animated by a follower force. Although this problem is already treated comprehensively in the literature, our approach will be benchmarked with the past results to provide a robust and efficient solver. We then investigate the elastohydrodynamics of active filaments in scenarios that coupled mechanics of fluid and structure plays a crucial role, for instance the collective dynamics of ciliary arrays in a channel.

Chapter 7

Conclusion and Future work

In this thesis:

- We showed how at low Reynolds' numbers the nonlinear Navier-Stokes differential equations can be simplified into the linear Stokes equations. We then derived the Greens' function of the Stokes equations (also called Stokeslet) in the presence of a point force, which acts on the fluid at a specific location. In addition to the Stokeslet, other singularity solutions of the Stokes flow both for an unbounded flow as well as a flow passing over an infinite plane wall, are presented. For each case, we illustrate the flow around the singularity solutions using velocity contours, streamlines, and pressure contours.

- We employed the singularity solutions of the Stokes flow to investigate the hydrodynamic interactions between the slender bodies and the surrounding fluid. The distribution of appropriate singularities with unknown strength along the center-line of the filament can provide us with a series of linear equations. The information about the shape and velocity of the filament at each cross-section contributes to the series of linear equations to determine the unknown strengths of singularity solutions. As a result, the hydrodynamic forces exerted on each cross-section of the filament can readily be determined since they are exactly equal in magnitude but opposite in the direction of the singularities' strengths. With the appropriate choice of singular solutions, the motion of a slender filament in both an unbounded flow and near a rigid no-slip plane wall can be simulated.

- We presented a continuum rod model to capture the dynamics of the filaments, in which the hydrodynamic drag forces contribute to the rod equations in the form of external loads. We discretize the system of partial differential equations in space and time and solve them using the method of assembled matrices. As a

result, we present the procedure through which our hydrodynamic model combined with our computational rod equations can be integrated through time to interactively determine the shape of the filament. The computational rod model can also capture the buckling instabilities due to the presence of the follower forces. Therefore, a lot of interesting problems can be answered by the computational model we presented here.

- However, as an additional contribution we investigated the accuracy of the slender body theory in a few different scenarios; the motion of a straight rod in free stream, the motion of a straight rod near a no-slip wall, and the flow passing a rod attached to a no-slip wall. For each case, the total hydrodynamic drag forces exerted on the rod are compared with the CFD results. In all cases, the results verified that the total force exponentially decreases as the length-over-radius (slenderness) ratio increases. In the case of swimming in unbounded flow, we obtained $\sim 7\%$ and $\sim 2\%$ error for the slenderness ratios of $\eta = 20$ and $\eta = 100$, respectively. However, the results of the rod moving near the plane wall suggest that as the slender object is closer to the wall, higher hydrodynamic force is exerted on it. More importantly, we found that W-SBT would fail in providing an accurate solution when the slender object is very close to the wall. For instance, when $\eta = 20$ we will have $\frac{h-a}{h} = 0.75$ where h is the gap between the center-line of the filament and the wall, and a is the radius. In this case, we obtained $\sim 22.5\%$ error between the W-SBT and CFD while the error decreases to $\sim 7\%$ for $\eta = 75$ where $\frac{h-a}{h} = 0.935$. In the near-wall swimming, in addition to the choice of $\eta \gg 1$, we should also ensure that $\frac{h-a}{h} \simeq 1$ to obtain a relatively more accurate solution.

Last but not least, it is worth mentioning that we did not investigate the effect of the curvature of the filament on the accuracy of the slender body theory. The prediction of the hydrodynamic force by SBT can be accompanied by higher error values when the filament is highly curved. Moreover, in the case of two or more filaments moving very close to each other, the same problem as we discussed in the previous section may happen to jeopardize the accuracy of the slender body formulations. In such problems, using other hydrodynamic models such as the boundary element method (BEM) and immersed boundary method (IBM) is recommended. Although they may provide more accurate solutions but their computational costs compared to the SBT would not be negligible. A thorough survey of the accuracy of hydrodynamic models versus their computational cost can be conducted as future work.

Bibliography

[1] BA Afzelius. "Cilia-related diseases". In: *The Journal of Pathology: A Journal of the Pathological Society of Great Britain and Ireland* 204.4 (2004), pp. 470–477.

[2] BA Afzelius. "Cilia-related diseases". In: *The Journal of Pathology: A Journal of the Pathological Society of Great Britain and Ireland* 204.4 (2004), pp. 470–477.

[3] John Baillieul and Mark Levi. "Rotational elastic dynamics". In: *Physica D: Nonlinear Phenomena* 27.1-2 (1987), pp. 43–62.

[4] GK Batchelor. "Slender-body theory for particles of arbitrary cross-section in Stokes flow". In: *Journal of Fluid Mechanics* 44.3 (1970), pp. 419–440.

[5] Leif E Becker, Stephan A Koehler, and Howard A Stone. "On self-propulsion of micro-machines at low Reynolds number: Purcell's three-link swimmer". In: *Journal of fluid mechanics* 490 (2003), pp. 15–35.

[6] Alejandro Jesús Bermejo-Valdés, Alexander Ariel Padrón-González, and Jessica Archer-Jiménez. "Ciliary Dysfunction Secondary to COVID-19. Explanation of the Pathogenesis From Analysis of Human Interactome With Sars-Cov-2 Proteome". In: (2020).

[7] Eloıse Bertiaux and Philippe Bastin. "Dealing with several flagella in the same cell". In: *Cellular Microbiology* 22.3 (2020), e13162.

[8] JR Blake. "A note on the image system for a Stokeslet in a no-slip boundary". In: *Mathematical Proceedings of the Cambridge Philosophical Society*. Vol. 70. 2. Cambridge University Press. 1971, pp. 303–310.

[9] JR Blake and AT Chwang. "Fundamental singularities of viscous flow". In: *Journal of Engineering Mathematics* 8.1 (1974), pp. 23–29.

[10] Carlo L Bottasso and Marco Borri. "Integrating finite rotations". In: *Computer Methods in Applied Mechanics and Engineering* 164.3-4 (1998), pp. 307–331.

[11] Carlo L Bottasso and Marco Borri. "Integrating finite rotations". In: *Computer Methods in Applied Mechanics and Engineering* 164.3-4 (1998), pp. 307–331.

[12] Christopher Brennen and Howard Winet. "Fluid mechanics of propulsion by cilia and flagella". In: *Annual Review of Fluid Mechanics* 9.1 (1977), pp. 339–398.

[13] Jason M Brown and George B Witman. "Cilia and diseases". In: *Bioscience* 64.12 (2014), pp. 1126–1137.

[14] Brato Chakrabarti and David Saintillan. "Spontaneous oscillations, beating patterns, and hydrodynamics of active microfilaments". In: *Physical Review Fluids* 4.4 (2019), p. 043102.

[15] Jintai Chung and GM1223971 Hulbert. "A time integration algorithm for structural dynamics with improved numerical dissipation: the generalized-α method". In: (1993).

[16] Ricardo Cortez. "Regularized stokeslet segments". In: *Journal of Computational Physics* 375 (2018), pp. 783–796.

[17] Ricardo Cortez. "The method of regularized Stokeslets". In: *SIAM Journal on Scientific Computing* 23.4 (2001), pp. 1204–1225.

[18] Ricardo Cortez, Lisa Fauci, and Alexei Medovikov. "The method of regularized Stokeslets in three dimensions: analysis, validation, and application to helical swimming". In: *Physics of Fluids* 17.3 (2005), p. 031504.

[19] Ricardo Cortez and Douglas Varela. "A general system of images for regularized Stokeslets and other elements near a plane wall". In: *Journal of Computational Physics* 285 (2015), pp. 41–54.

[20] R. G. Cox. "The motion of long slender bodies in a viscous fluid Part 1. General theory". In: *Journal of Fluid Mechanics* 44.4 (1970), pp. 791–810. DOI: 10.1017/S002211207000215X.

[21] Camilo Cruz, Francisco Chinesta, and Gilles Regnier. "Review on the Brownian dynamics simulation of bead-rod-spring models encountered in computational rheology". In: *Archives of Computational Methods in Engineering* 19.2 (2012), pp. 227–259.

[22] Blaise Delmotte, Eric Climent, and Franck Plouraboué. "A general formulation of Bead Models applied to flexible fibers and active filaments at low Reynolds number". In: *Journal of Computational Physics* 286 (2015), pp. 14–37.

[23] Olivia Du Roure et al. "Dynamics of flexible fibers in viscous flows and fluids". In: *Annual Review of Fluid Mechanics* 51 (2019), pp. 539–572.

[24] Jens Elgeti and Gerhard Gompper. "Emergence of metachronal waves in cilia arrays". In: *Proceedings of the National Academy of Sciences* 110.12 (2013), pp. 4470–4475.

[25] Jens Elgeti and Gerhard Gompper. "Emergence of metachronal waves in cilia arrays". In: *Proceedings of the National Academy of Sciences* 110.12 (2013), pp. 4470–4475.

[26] Ali Ahmad Farooq, D Tripathi, and Thanaa Elnaqeeb. "On the propulsion of micropolar fluid inside a channel due to ciliary induced metachronal wave". In: *Applied Mathematics and Computation* 347 (2019), pp. 225–235.

[27] Soheil Fatehiboroujeni. "Inverse Approaches for Identification of Constitutive Laws of Slender Structures Motivated by Application to Biological Filaments". PhD thesis. 2018, p. 142. ISBN: 978-0-438-10859-2. URL: https://search.proquest.com/docview/2070391920?accountid=14515.

[28] Soheil Fatehiboroujeni, Arvind Gopinath, and Sachin Goyal. "Nonlinear Oscillations Induced by Follower Forces in Prestressed Clamped Rods Subjected to Drag". In: *Journal of Computational and Nonlinear Dynamics* 13.12 (2018).

[29] Soheil Fatehiboroujeni, Harish J Palanthandalam-Madapusi, and Sachin Goyal. "Computational rod model with user-defined nonlinear constitutive laws". In: *Journal of Computational and Nonlinear Dynamics* 13.10 (2018).

[30] M. Fritzsche et al. "Self-organizing actin patterns shape membrane architecture but not cell mechanics". In: *Nature Communications* 8 (Nov. 2017), p. 14347. URL: https://doi.org/10.1038/ncomms14347.

[31] AR Galper, T Miloh, and M Spector. "Higher order slender body theory". In: *Analytical and Computational Methods in Scattering and Applied Mathematics, F. Santosa and I. Stakgold, eds., CRC Press, London, Boca Raton, FL* (2000), pp. 111–121.

[32] Mattia Gazzola et al. "Forward and inverse problems in the mechanics of soft filaments". In: *Royal Society open science* 5.6 (2018), p. 171628.

[33] ERIC A. GILLIES et al. "Hydrodynamic propulsion of human sperm". In: *Journal of Fluid Mechanics* 625 (2009), pp. 445–474.

[34] Jason I Gobat. *The dynamics of geometrically compliant mooring systems.* Tech. rep. MASSACHUSETTS INST OF TECH CAMBRIDGE, 2000.

[35] Arvind Gopinath and Ashok S Sangani. "Elastohydrodynamical instabilities of active filaments, arrays and carpets analyzed using slender body theory". In: *bioRxiv* (2020).

[36] Alain Goriely and Michael Tabor. "The nonlinear dynamics of filaments". In: *Nonlinear Dynamics* 21.1 (2000), pp. 101–133.

[37] Benjamin Gorissen et al. "Artificial Pneumatic Cilia". In: *Atlas of Cilia Bioengineering and Biocomputing* (2018), p. 61.

[38] Sachin Goyal. "A dynamic rod model to simulate mechanics of cables and DNA". PhD thesis. 2006.

[39] Sachin Goyal, Noel C Perkins, and Christopher L Lee. "Nonlinear dynamics and loop formation in Kirchhoff rods with implications to the mechanics of DNA and cables". In: *Journal of Computational Physics* 209.1 (2005), pp. 371–389.

[40] James Gray and GJ Hancock. "The propulsion of sea-urchin spermatozoa". In: *Journal of Experimental Biology* 32.4 (1955), pp. 802–814.

[41] Jeffrey S. Guasto, Roberto Rusconi, and Roman Stocker. "Fluid Mechanics of Planktonic Microorganisms". In: *Annual Review of Fluid Mechanics* 44.1 (2012), pp. 373–400.

[42] Shay Gueron and Konstantin Levit-Gurevich. "The three-dimensional motion of slender filaments". In: *Mathematical methods in the applied sciences* 24.17-18 (2001), pp. 1577–1603.

[43] Shay Gueron and Nadav Liron. "Ciliary motion modeling, and dynamic multicilia interactions". In: *Biophysical journal* 63.4 (1992), pp. 1045–1058.

[44] Srinivas Hanasoge, Peter J Hesketh, and Alexander Alexeev. "Microfluidic pumping using artificial magnetic cilia". In: *Microsystems & nanoengineering* 4.1 (2018), pp. 1–9.

[45] Jonathan JL Higdon. "A hydrodynamic analysis of flagellar propulsion". In: *Journal of Fluid Mechanics* 90.4 (1979), pp. 685–711.

[46] Inés Ibañez-Tallon, Nathaniel Heintz, and Heymut Omran. "To beat or not to beat: roles of cilia in development and disease". In: *Human molecular genetics* 12.suppl_1 (2003), R27–R35.

[47] COMSOL Inc. *About the Stationary Solver in COMSOL.* URL: `https://doc.comsol.com/5.5/doc/com.comsol.help.comsol/comsol_ref_solver.27.096.html`.

[48] Taylor Geoffrey Ingram. "Analysis of the swimming of microscopic organisms". In: (1951).

[49] Takashi Ishikawa. "Axoneme structure from motile cilia". In: *Cold Spring Harbor perspectives in biology* 9.1 (2017), a028076.

[50] Kenta Ishimoto and Eamonn A Gaffney. "Boundary element methods for particles and microswimmers in a linear viscoelastic fluid". In: *Journal of Fluid Mechanics* 831 (2017), pp. 228–251.

[51] MK Jawed and Pedro M Reis. "Dynamics of a flexible helical filament rotating in a viscous fluid near a rigid boundary". In: *Physical Review Fluids* 2.3 (2017), p. 034101.

[52] RE Johnson and CJ Brokaw. "Flagellar hydrodynamics. A comparison between resistive-force theory and slender-body theory". In: *Biophysical journal* 25.1 (1979), pp. 113–127.

[53] Robert E Johnson. "An improved slender-body theory for Stokes flow". In: *Journal of Fluid Mechanics* 99.2 (1980), pp. 411–431.

[54] Mithun Kanchan and Ranjith Maniyeri. "Numerical simulation of buckling and asymmetric behavior of flexible filament using temporal second-order immersed boundary method". In: *International Journal of Numerical Methods for Heat & Fluid Flow* (2019).

[55] Panayiota Katsamba and Eric Lauga. "Propulsion by stiff elastic filaments in viscous fluids". In: *Physical Review E* 99.5 (2019), p. 053107.

[56] Joseph B Keller and Sol I Rubinow. "Slender-body theory for slow viscous flow". In: *Journal of Fluid Mechanics* 75.4 (1976), pp. 705–714.

[57] Stephen M King and Winfield S Sale. "Fifty years of microtubule sliding in cilia". In: *Molecular biology of the cell* 29.6 (2018), pp. 698–701.

[58] Gustav Kirchhoff. "Uber das Gleichgewicht und die Bewegung eines unendlich dunnen elastischen Stabes". In: *J. reine angew. Math.* 56 (1859), pp. 285–313.

[59] Lyndon Koens and Eric Lauga. "The boundary integral formulation of Stokes flows includes slender-body theory". In: *Journal of Fluid Mechanics* 850 (2018).

[60] Eric Lauga. "Bacterial Hydrodynamics". In: *Annual Review of Fluid Mechanics* 48.1 (2016), pp. 105–130.

[61] Eric Lauga and Thomas R Powers. "The hydrodynamics of swimming microorganisms". In: *Reports on Progress in Physics* 72.9 (2009), p. 096601.

[62] Mark Levi. "Composition of rotations and parallel transport". In: *Nonlinearity* 9.2 (1996), p. 413.

[63] James Lighthill. "Flagellar hydrodynamics". In: *SIAM review* 18.2 (1976), pp. 161–230.

[64] Todd D Lillian et al. "A multiscale dynamic model of DNA supercoil relaxation by topoisomerase IB". In: *Biophysical journal* 100.8 (2011), pp. 2016–2023.

[65] Feng Ling, Hanliang Guo, and Eva Kanso. "Instability-driven oscillations of elastic microfilaments". In: *Journal of The Royal Society Interface* 15.149 (2018), p. 20180594.

[66] Maciej Lisicki. "Four approaches to hydrodynamic Green's functions–the Oseen tensors". In: *arXiv preprint arXiv:1312.6231* (2013).

[67] Bin Liu, Kenneth S Breuer, and Thomas R Powers. "Helical swimming in Stokes flow using a novel boundary-element method". In: *Physics of Fluids* 25.6 (2013), p. 061902.

[68] Meiying Liu et al. "Recent developments in polydopamine: an emerging soft matter for surface modification and biomedical applications". In: *Nanoscale* 8.38 (2016), pp. 16819–16840.

[69] Yi Man, Lyndon Koens, and Eric Lauga. "Hydrodynamic interactions between nearby slender filaments". In: *EPL (Europhysics Letters)* 116.2 (Oct. 2016), p. 24002. DOI: 10.1209/0295-5075/116/24002. URL: https://doi.org/10.1209/0295-5075/116/24002.

[70] Yi Man, Feng Ling, and Eva Kanso. "Cilia oscillations". In: *Philosophical Transactions of the Royal Society B* 375.1792 (2020), p. 20190157.

[71] Pranay Mandal et al. "Magnetic active matter based on helical propulsion". In: *Accounts of Chemical Research* 51.11 (2018), pp. 2689–2698.

[72] M Cristina Marchetti et al. "Hydrodynamics of soft active matter". In: *Reviews of Modern Physics* 85.3 (2013), p. 1143.

[73] Oana Marin. "Boundary integral methods for Stokes flow: Quadrature techniques and fast Ewald methods". PhD thesis. KTH Royal Institute of Technology, 2012.

[74] Edoardo Milana et al. "Metachronal patterns in artificial cilia for low Reynolds number fluid propulsion". In: *Science Advances* 6.49 (2020), eabd2508.

[75] Debasmita Mondal, Ronojoy Adhikari, and Prerna Sharma. "Internal friction controls active ciliary oscillations near the instability threshold". In: *Science advances* 6.33 (2020), eabb0503.

[76] Daniel Needleman and Zvonimir Dogic. "Active matter at the interface between materials science and cell biology". In: *Nature Reviews Materials* 2 (July 2017). Review Article, 17048 EP -. URL: http://dx.doi.org/10.1038/natrevmats.2017.48.

[77] C Ni et al. "Optical determination of the flexural rigidity of carbon nanotube ensembles". In: *Applied Physics Letters* 92.17 (2008), p. 173106.

[78] Carl Wilhelm Oseen. "Neuere methoden und ergebnisse in der hydrodynamik". In: *Leipzig: Akademische Verlagsgesellschaft mb H.* (1927).

[79] Rajasekharreddy Pala et al. "The roles of primary cilia in cardiovascular diseases". In: *Cells* 7.12 (2018), p. 233.

[80] C Pozrikidis. "Shear flow over cylindrical rods attached to a substrate". In: *Journal of fluids and structures* 26.3 (2010), pp. 393–405.

[81] C Pozrikidis. "Shear flow past slender elastic rods attached to a plane". In: *International Journal of Solids and Structures* 48.1 (2011), pp. 137–143.

[82] Constantine Pozrikidis. *A practical guide to boundary element methods with the software library BEMLIB*. CRC Press, 2002.

[83] Constantine Pozrikidis et al. *Boundary integral and singularity methods for linearized viscous flow*. Cambridge University Press, 1992.

[84]   Constantine Pozrikidis. *Introduction to theoretical and computational fluid dynamics*. Oxford university press, 2011.

[85]   Samira Goli Pozveh, Albert Bae, and Azam Gholami. "Resistive force theory and wave dynamics in swimming flagellar apparatus isolated from C. reinhardtii". In: *Soft Matter* (2020).

[86]   Sriram Ramaswamy. "Active matter". In: *Journal of Statistical Mechanics: Theory and Experiment* 2017.5 (2017), p. 054002.

[87]   Xiaoting Ren et al. "A Self-Cleaning Mucus-like and Hierarchical Ciliary Bionic Surface for Marine Antifouling". In: *Advanced Engineering Materials* 22.5 (2020), p. 1901198.

[88]   Ingmar H Riedel-Kruse et al. "How molecular motors shape the flagellar beat". In: *HFSP journal* 1.3 (2007), pp. 192–208.

[89]   Olinde Rodrigues. *Des lois géométriques qui régissent les déplacements d'un système solide dans l'espace: et de la variation des cordonnées provenant de ces déplacements considérés indépendamment des causes qui peuvent les produire*. 1840.

[90]   Taryn Saggese et al. "Development of a method for the measurement of primary cilia length in 3D". In: *Cilia* 1.1 (2012), p. 11.

[91]   Manfred Schliwa and Günther Woehlke. "Molecular motors". In: *Nature* 422.6933 (2003), pp. 759–765.

[92]   Juan C Simo, Jerrold E Marsden, and PS Krishnaprasad. "The Hamiltonian structure of nonlinear elasticity: the material and convective representations of solids, rods, and plates". In: *Archive for Rational Mechanics and Analysis* 104.2 (1988), pp. 125–183.

[93]   Anu Sironen et al. "Sperm defects in primary ciliary dyskinesia and related causes of male infertility". In: *Cellular and Molecular Life Sciences* 77.11 (2020), pp. 2029–2048.

[94]   David J Smith. "A boundary element regularized Stokeslet method applied to cilia-and flagella-driven flow". In: *Proceedings of the Royal Society A: Mathematical, Physical and Engineering Sciences* 465.2112 (2009), pp. 3605–3626.

[95]   Saverio E Spagnolie and Eric Lauga. "Hydrodynamics of self-propulsion near a boundary: predictions and accuracy of far-field approximations". In: *Journal of Fluid Mechanics* 700 (2012), pp. 105–147.

[96]   Daniel See Wai Tam. "Motion at low Reynolds number". PhD thesis. Massachusetts Institute of Technology, 2008.

[97]   Jaap M.J. den Toonder and Patrick R. Onck. "Microfluidic manipulation with artificial/bioinspired cilia". In: *Trends in Biotechnology* 31.2 (2013), pp. 85–91. ISSN: 0167-7799.

[98] Jaap MJ den Toonder and Patrick R Onck. "Microfluidic manipulation with artificial/bioinspired cilia". In: *Trends in biotechnology* 31.2 (2013), pp. 85–91.

[99] Anna-Karin Tornberg and Michael J Shelley. "Simulating the dynamics and interactions of flexible fibers in Stokes flows". In: *Journal of Computational Physics* 196.1 (2004), pp. 8–40.

[100] Jyothish Vidyadharan. "The mechanism of self-organized beating of cilia". In: (2014).

[101] Benjamin J Walker et al. "A regularised slender-body theory of non-uniform filaments". In: *Journal of Fluid Mechanics* 899 (2020), A3.

[102] Benjamin J Walker et al. "Filament mechanics in a half-space via regularised Stokeslet segments". In: *Journal of Fluid Mechanics* 879 (2019), pp. 808–833.

[103] Christian Wollblad. *How to Set Up a Mesh in COMSOL Multiphysics® for CFD Analyses*. 2018. URL: https://www.comsol.com/blogs/how-to-set-up-a-mesh-in-comsol-multiphysics-for-cfd-analyses/.

[104] Ling Xu and Yi Jiang. "Mathematical modeling of mucociliary clearance: a mini-review". In: *Cells* 8.7 (2019), p. 736.

[105] Hai-Zhuan Yuan et al. "A momentum exchange-based immersed boundary-lattice Boltzmann method for simulating a flexible filament in an incompressible flow". In: *Computers & Mathematics with Applications* 67.5 (2014), pp. 1039–1056.

[106] Shuaizhong Zhang et al. "A concise review of microfluidic particle manipulation methods". In: *Microfluidics and Nanofluidics* 24.4 (2020), pp. 1–20.

[107] Shuaizhong Zhang et al. "Anti-Biofouling and Self-Cleaning Surfaces Featured with Magnetic Artificial Cilia". In: *ACS Applied Materials & Interfaces* (2020).

[108] Shuaizhong Zhang et al. "Removal of microparticles by ciliated surfaces—an experimental study". In: *Advanced Functional Materials* 29.6 (2019), p. 1806434.